The development of a thermoelectric generator (TEG) concept for recycling waste heat into electricity

Justin J. Riggio

Co-Supervisors: Professor Frank Mucciardi and Professor Ferri Hassani

A thesis submitted to McGill University in partial fulfillment of the requirements for the degree of M.Eng.

Mining and Materials Engineering
McGill University
Montreal, Québec, Canada
December 2019

Abstract

There is a significant amount of waste heat from industrial processes in the form of liquid or gaseous streams. With a growing demand for electrical power, there is a need for solutions to make use of this heat and increase the overall energy efficiency of the processes in question. Although the most practical solution may be to recuperate the waste heat for heating and/or cooling purposes, its transformation into electricity allows for versatility in its end-use. The thermoelectric generator (TEG) presented in this work consists of heat pipes to capture and concentrate the waste heat, coupled with thermoelectric modules to convert some of the heat directly into electricity. A bench-top prototype was designed and built as a proof-of-concept. The experimental testing of the prototype involved the measurement of power output to a load as a function of the temperature and flow rate of the inlet air, which represented the waste heat stream. The efficiency as a function of temperature and flow rate was then obtained by estimating the heat captured by the TEG using an empirical relation for a cylinder in a cross-flow. The results obtained for power output compared well with a model developed for thermoelectric module performance in both a simplified and detailed approach. However, as the steady-state temperature measurements from the hot-side and cold-side of the thermoelectric modules were input to the model, the effect of the heat pipes was not fully accounted for. There are factors, including thermal contact resistance at the interfaces and heat transfer limitations of the heat pipes that can be further investigated and improved in order to maximize the power per unit area of the TEG. Furthermore, recommendations for industrial application of this concept are discussed on the subject of performance optimization when scaling up and life-cycle analysis. To conclude, a strategy for the further development of this concept is presented.

Abrégé

Les procédés industriels proiduisent une quantité importante de chaleur résiduelle sous forme d'écoulements liquide ou gazeux. Dû à la demande croissante en puissance électrique, il est nécessaire de trouver des solutions pour utiliser cette chaleur afin d'augmenter l'efficacité des procédés en question. Par exemple, la chaleur résiduelle pourrait être récupérée pour le chauffage et/ou le refroidissment. Cependant, la transformation de cette chaleur en electricité permettrait une plus grande polyvalence en terme d'utilisation finale. La génératrice thermoélectrique présentée dans ce mémoire est composée de caloducs pour capter et concentrer la chaleur résiduelle couplés de modules thermoélectriques afin de convertir une portion de la chaleur directement en énergie électrique. Un prototype a été conçu et construit afin de valider le concept. Le prototype a été testé en obtenant la puissance électrique en fonction de la température et du débit de l'air entrant, qui répresentait la chaleur résiduelle. L'efficacité énergétique en fonction de la température et du débit a été calculée par l'estimation de la chaleur capturée par la génératrice avec une relation empirique pour un cylindre soumis à un débit tranversal. Les résultats sont comparables à ceux obtenus à partir d'un modèle conçu pour la performance des modules thermoélectriques. Par contre, puisque le modèle requiert des mesures de température uniquement des côtés chaud et froid des modules thermoélectriques, l'effet complet des caloducs n'était pas pris en compte. Cependant, des facteurs comme la résistance de contact thermique et les limitations de transfert de chaleur pourraient être explorés en détail afin d'augmenter la puissance par superficie de la génératrice thermoélectrique. De plus, des recommandations sont décrites pour l'application industrielle de ce concept, plus précisément au sujet de l'optimisation de la performance avec accroissement d'échelle et de l'analyse du cycle de vie. En conclusion, une stratégie potentielle pour le développement de cette génératrice thermoélectrique est presentée.

Acknowledgments

First and foremost, I would like to extend my gratitude to professor Frank Mucciardi. He has been such an inspirational mentor to me and I consider myself very fortunate to have the opportunity to work with him. His passion for realistic and practical solutions to problems of all sort has been truly enlightening. I would also like to thank professor Ferri Hassani. I am grateful for his support and patience throughout the building of this work. Many thanks to others in the department for the invaluable teachings and encouragement along the way, especially Terry, and Barbara. Thanks to Maurizio, Lindsey, Samantha and Philippe, as undergraduates in the department of mechanical engineering, the work they accomplished on the Capstone project was an essential contribution to the project. I would like to thank Roberto for all his technical expertise with the fabrication of the prototype. Also thanks to Dr.Carriere, for his insight on thermocouples and the meticulous fabrication of them. I would like to thank Robert, Frank C. and Joe for all the advice on technical aspects during the experimental work and lending me the tools I required for it. Also thanks to Gauthier, for kindly providing assistance with modeling and other aspects during his undergraduate studies. I would like to thank Aleksander for his warm welcome in Oslo and the fruitful late night chats about material science. Thanks to Dr.Lee for his insight on the modeling of thermoelectric devices. And to Dr.Amiri, for her help on modeling turbulence. Finally, a special thanks to Michael for lending his expertise on heat transfer and fluid dynamics as well his advice on the experimental set-up.

To my mother and father, as well as my immediate and extended family, I am so thankful for the presence of all of you in my life. Your love and support throughout has been vital. To Sarah, I cannot thank you enough for such positive support in my endeavours. The continuous inspiration you bring to life is truly a blessing.

Dedicated to sustainable energy for all

Contents

List of Figures and Tables

Nomenclature

α	Seebeck coefficient [VK^{-1}]
ΔT	temperature difference [°C]
ΔV	potential difference or Voltage [V]
η	efficiency [%]
ν_f	kinematic viscosity at film temperature [m$^2 s^{-1}$]
π	Peltier coefficient [V]
Pr_f	Prandlt number at film temperature
ρ	electrical resistivity [Ωm]
σ	electrical conductivity [AV$^{-1} m^{-1}$]
τ	Thomson coefficient [VK^{-1}]
A	area [m^2]
C	thermal conductance [WK^{-1}]
d	hydraulic diameter[m]
E	energy [J]
E_F	Fermi level [J]
$F(E)$	Fermi function
h	heat transfer coefficient[Wm$^{-2} K^{-1}$]
I	current [A]
K	Boltzmann's constant[JK^{-1}]
k	thermal conductivity [Wm$^{-1} K^{-1}$]
k_f	thermal conductivity of the fluid [Wm$^{-1} K^{-1}$]
L	length [m]
Nu	Nusselt number
Q	heat flow [Js^{-1}]
Q''	heat flux [Wm^{-2}]
R	electrical resistance [Ω]
u_∞	bulk velocity of the fluid [ms^{-1}]
ZT	dimensionless figure-of-merit
T	absolute temperature [K]

Chapter 1

Introduction

1.1 A brief history

Alessandro Volta (1745-1827) was the first to correctly explain the phenomenon of direct conversion of heat into electricity through experimentation at the University of Pavia [16][17]. He set-up an experiment where a dead frog's hind legs were submerged in a glass of water and the back spine in another as shown in Figure 1.1. He observed violent contractions of the frog's muscles for some conductors and found that the water in the two glasses needed to be at a different temperature for this phenomena to occur. After further work, he correctly concluded that an electromotive force or voltage can be generated from the temperature difference between the two junctions. [1]

Figure 1.1: An adapted sketch of Volta's frog experiment [1]

Thomas Seebeck (1770-1831) observed, twenty years later, that a closed circuit made of two dissimilar metals deflected a nearby magnetic compass when the two junctions of the circuit were held at different temperatures. He called the phenomenon "thermomagnetism", which led him to suggest that the Earth's magnetic field is present due to the temperature difference between the two poles and the equator [1]. Although Seebeck did not identify the cause of the magnetic field implicitly, [1], at this time, there had been significant advances in the field of electromagnetism, through the theoretical and experimental work of many researchers, notably Joseph Priestly (1733-1804), Charles-Augustin de Coulomb (1736-1806) and later Michael Faraday (1791-1867)[18]. Today, the phenomena of generating a voltage by a temperature gradient is commonly referred to as the Seebeck effect. Nevertheless, Volta was commemorated for his discovery in 2005 by the International Thermoelectric Academy[19].

Together, Hans Ørsted (1777-1851) and Jean-Baptiste Fourier (1768-1830) were considered the first to build a thermoelectric device which was similar to a voltaic pile, by combining three bars of bismuth (Bi) with three bars of antimony (Sb) forming a circuit [20]. John Rayleigh (1842-1919) was considered to be the first to propose the concept of heat-to-electricity conversion, using the Seebeck effect for power generation with circuits similar to those built by Ørsted and Fourier [21]. In the late 19^{th} century, thermoelectric devices were designed and built consisting of conductors that were arranged to be thermally in parallel and electrically in series with hot gases or liquids used as sources of heat. Since the purpose of these devices are to generate power, they were called thermoelectric generators (TEGs). [1]

One of earliest demonstrations of a TEG was the “Clammond pile”, made of 3000 thermocouples, it was able to generate a maximum power output of about 200W over a fireplace by burning coke at a rate of about 10kg per hour [22]. In the first half of the 20^{th} century, there was significant progress in semiconductor technology which lead to the fabrication of thermoelectric devices with higher efficiencies. One example of this advancement is the work of Maria Telkes (1900-1995), who was able to fabricate a thermoelectric generator based on PbS and ZnSb with a conversion efficiency of about 5% with ΔT$\approx 400K$. Another example is in the 1950s, when the Soviet Union designed and commercialized a TEG, made of ZnSb/Constantan couples, to power radios in remote areas from heat supplied by kerosene lamps.[1]

Although there was indeed evidence of progress, the efficiency of TEGs were not significantly increasing, and therefore, the research in thermoelectricity for power production shifted towards niche applications. In space missions, since photovoltaics were not always sufficient to power on-board instrumentation, TEGs were developed and implemented using radioisotopes, such as Pu, for a slowly decaying source of heat [1]. The Transit 5BN-1, launched in 1963 was the first satellite using a TEG for primary power [23]. After successful implementation, further developments were being made by US space programs. The Voyager 1 and 2, launched by NASA in 1977, use a TEG with a starting efficiency of 6.6% and are still operational after over 40 years of use [24].

In the late 20th century, significant progress was made in research and development which lead to promising insight for the direction of thermoelectrics. In the 1990s, physicists Mildred Dresselhaus and L.D Hicks of Massachusetts's Institute of Technology proposed to use nanomaterials in order to increase the efficiency of semiconductors for higher thermal-to-electrical conversion [25]. Over 15 years from the year 2000, the evidence of growth in the field is shown by the increase in publications from around 500 to more than 2500 annually [26].

Another interesting and rather more recent approach to convert heat into electricity is by using pyroelectric materials. They differ from thermoelectric materials as they use temperature fluctuations to produce electric potential instead of temperature gradients. When a pyroelectric sample is heated, the lattice vibrations cause a rearrangement of its crystal structure in such a way that it leads to less free charges being bound to the surface. If this sample is under open circuit conditions, an electric potential is generated across the sample. The theoretical thermal-to-electrical efficiency is significantly closer to the ideal Carnot efficiency compared to thermoelectric materials. However, it would require maintaining precise temperature variations with high frequency which may not be as practical for industrial waste heat recovery. A rather interesting application can be to power devices in the nanoscale and/or microscale, at which it may be easier to obtain the required conditions. Nonetheless, the combination of pyroelectric devices with thermoelectric devices and/or solar cells can form a promising hybrid technology with excellent conversion efficiencies. [27, 28, 29]

Although there is indeed a challenge in maintaining a large temperature gradient across thermoelectric devices, the aim of this work is to contribute towards a cost-effective approach to do so and ultimately develop a competitive option for a wide range of industrial waste heat scenarios.

1.2 Thermoelectric phenomena

The science governing thermoelectricity and the ability to engineer thermoelectric devices relies on the understanding of thermoelectric phenomena. There are three important phenomena to consider, namely, the Seebeck effect, the Peltier effect and the Thomson effect. A brief physical and mathematical description will follow.

1.2.1 The Seebeck effect

The Seebeck effect is an electromotive force or voltage that can be generated when a temperature gradient is imposed between the junctions of two dissimilar electrical conductors.

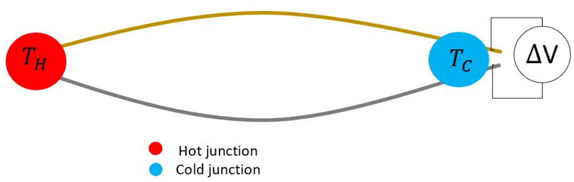

Figure 1.2: A schematic of the Seebeck effect

The constant of proportionality between the temperature gradient (ΔT) and voltage (ΔV) is the differential Seebeck coefficient (α_e).

$$\alpha_e = \frac{\Delta V}{\Delta T} \tag{1.1}$$

$$\alpha_e = \alpha_p - \alpha_n \tag{1.2}$$

The subscripts n and p refer to two dissimilar conductors one with a negative and positive Seebeck coefficient respectively. A practical use of this phenomena is for temperature measurements. For example, a type T thermocouple is made of a copper wire (p-type) and a constantan wire (n-type), together their differential Seebeck coefficient is approximately 40 μV/K [2].

1.2.2 The Peltier effect

Jean-Charles-Athanase Peltier (1785-1845) discovered that when a current is forced through an isothermal junction of dissimilar conductors, the junction is heated or cooled depending on the direction of the current. He tried to explain this by correlating the phenomenon to Joule heating. Heinrich Lenz (1804-1865) was able to prove that it was not related to the Joule effect and that it is its' own physical phenomenon, later called the Peltier effect [1]. The Peltier effect occurs as additional heat is absorbed or released when a current is forced through a junction between two dissimilar electrical conductors. The Peltier coefficient is defined as the heat released or absorbed per unit of time (Q) at the junction over the current flowing though the junction (I)[2].

$$\pi_e = \frac{Q}{I} \tag{1.3}$$

$$\pi_e = \pi_p - \pi_n \tag{1.4}$$

The Peltier effect is typically exploited for devices used for cooling applications. Although this effect is important as it will be used later mathematically for modeling purposes, this work will not go further into the use of this effect as the topic at hand is focused on power generation.

1.2.3 The Thomson effect

William Thomson (1824-1907), also known as Lord Kelvin, did a mathematical analysis of electricity and using a formulation of the first and second law of thermodynamics, he predicted a third thermoelectric effect. This occurs as current flows in a homogeneous electrical conductor subject to a temperature gradient and heat is absorbed or released depending on the mutual direction of the current and temperature gradient. It is now known as the Thomson effect, and is expressed by the Thomson coefficient[15]:

$$\tau = \frac{dQ/dx}{I \cdot dT/dx} \tag{1.5}$$

Where the numerator describes the heat absorbed or released per unit time and unit volume (1-d in the case of Eq. 1.5).

Later, he derived mathematical relations between the thermoelectric coefficients which are known as the Kelvin relations[1]:

$$\pi_e = \alpha_e \cdot T \tag{1.6}$$

and

$$\tau_a - \tau_b = T \cdot \frac{d\alpha_e/dx}{dT} \tag{1.7}$$

The subscripts a and b refer to two dissimilar conductors. Overall, this is an indication that the same thermoelectric materials can either produce power when subject to a temperature gradient or pump heat by applying a current [2].

1.3 The mechanisms behind thermoelectricity

In the free electron theory of metals, electrons are confined to states in specific bands of energy, separated by band gaps. The probability of an electron being confined to a certain energy state can be determined by quantum mechanics. There is a particular energy, commonly referred to as the Fermi level, at which there is a 50% probability of a state being filled. It is the states close to the Fermi level that are responsible for electrical transport phenomena. If the Fermi level is close to the conduction band, the carriers have a positive effective mass and regarded as quasi-free electrons, however if it is close to the valence band, the carriers behave as if they have a negative effective mass and thus widely regarded as holes.[2]

A semiconductor has an electronic band gap between the valence band and the next available energy band, the conduction band. With enough energy, an electron in the valence band can be excited to an available state in the conduction band, which would leave a hole in the valence band. [30]

The Fermi function gives the probability of occupation, in other words, the number of possible states that contain an electron. When the Fermi function is less than 1, the probability of an occupied state is less than 1, and therefore some states in the valence band remain empty. So when the Fermi function is larger than 0, the probability of occupation is finite and some electrons will occupy states in the conduction band. [31]

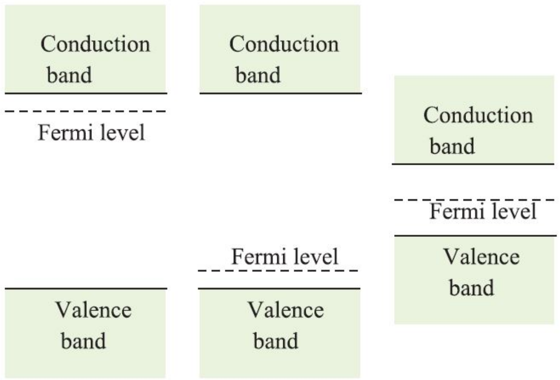

Figure 1.3: Energy band diagram for an n-type, p-type and an intrinsic semiconductor (such as Si)[2]

In a small device described by a conducting channel between two contacts, when a voltage is applied by a battery, the positive contact experiences a decrease in electrochemical potential to below equilibrium, and so the negative contact has an affinity to fill these empty levels with electrons. The positive contact, however, still has an affinity to be below this energy so pulls the electrons out to the external circuit, and this see-saw scenario continues which generally describes how current (number of charges per second) flows in a circuit. In the case of thermoelectric phenomena, the current is driven by a temperature gradient instead of an external voltage source. The shift from equilibrium would still be present in the device but due to the difference in temperature between the two contacts as the Fermi function is a function of temperature as well as the electrochemical potential of electrons or the Fermi level, E_F, in the case of equation 1.8. [32]

$$F(E) = \frac{1}{e^{\frac{(E-E_F)}{KT}} + 1} \tag{1.8}$$

There can be a shift in either direction from equilibrium, depending on the material, and thus current driven by temperature can flow in both directions. In other words, there can be more number of states that are occupied by electrons above the electrochemical potential than below and vice-versa. Conceptually, say particles are moving on a two-way street and there are more possible levels in one direction, this would result in a net flow in that direction, hence there are n-type and p-type materials. Although a p-type material is often described as conducting holes, this a conceptual tool used to keep track of the missing spots of unfilled bands but what is physically measured is always electrons flowing. [32]

Furthermore, when one end of a rod is heated and the other end is maintained at a lower temperature, depending on the type of thermoelectric material, the electrons or holes will move faster at the hot side, and diffuse towards the cold-side. An electric field is thus set-up across the rod due to concentration gradient of the charge carriers, and this is the basis of the Seebeck effect [3].

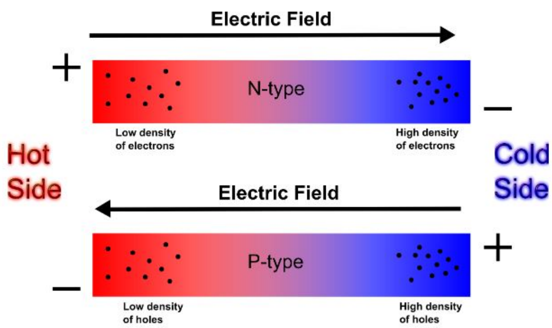

Figure 1.4: The Seebeck effect N- and p-type material as described by the diffusion of electrons and holes [3]

Overall, this was only a basic physical picture in order to describe why an electric potential is generated and how current flows due to temperature gradients using the modern theory of semi-conductor physics. It is therefore recommended to include other characteristics of electronic transport in semiconductors to complete the whole physical picture such as the wave function.

The transport properties for thermoelectric materials can be found from the relations between the gradients of the electric potential and temperature, and so, the electric current density and the heat flux density. To do so, the macroscopic theory of fluxes is extended by including an expression for the Seebeck effect. Then, using microscopic theory, based on the Boltzmann transport equation, expressions for the Seebeck coefficient, thermal conductivity and electrical conductivity can be obtained as a function of microscopic parameters such as the carrier charge concentration and effective mass of the electrons. [4] [33]

As an introduction to the next section is it important to note that the thermal conductivity has two components; the first part is from lattice vibrations, which is commonly explained by the traveling of phonons. The second is the electronic part, which involves electrons carrying heat. The electronic part of thermal conductivity, the electrical conductivity and Seebeck coefficient, all depend on the charge carrier concentration as seen in Figure 1.6. Therefore, these properties of thermoelectric materials are interdependent, and how well a thermoelectric material can convert heat into electricity can thus be quantified through a figure-of-merit.[2]

1.4 The Figure-of-Merit

The Seebeck and Peltier effects are reversible and would have similar characteristics to an ideal heat engine, however they are accompanied by the irreversible effects of electrical resistance and heat conduction [2].

The dimensionless figure-of-merit represents the goodness factor of a thermoelectric material. Abram Ioffe, who's work unveiled the theory of modern semi-conductor physics, introduced in 1949 the dimensionless figure-of-merit for a thermocouple [1].

$$ZT = \frac{\alpha_e^2}{CR} \cdot T \tag{1.9}$$

where R is the series electrical resistance and C is the thermal parallel conductance of the thermocouple.

Nowadays it is often described similarly as the following [34]:

$$ZT = \frac{\alpha_e^2 \cdot \sigma_e}{\kappa_e} \cdot T \tag{1.10}$$

where

$$\sigma_e = \sigma_p + \sigma_n \tag{1.11}$$

and

$$\kappa_e = \kappa_n + \kappa_p \tag{1.12}$$

describes the electrical and thermal conductivity respectively of the p-type and n-type material used in the thermocouple.

Although not as effective for practical use in power generation, single conductors can also be described using the figure-of-merit and can be determined through temperature-dependent measurement techniques of samples [35]. This can be used to compare different p and n- type materials as shown in Figure 1.5.

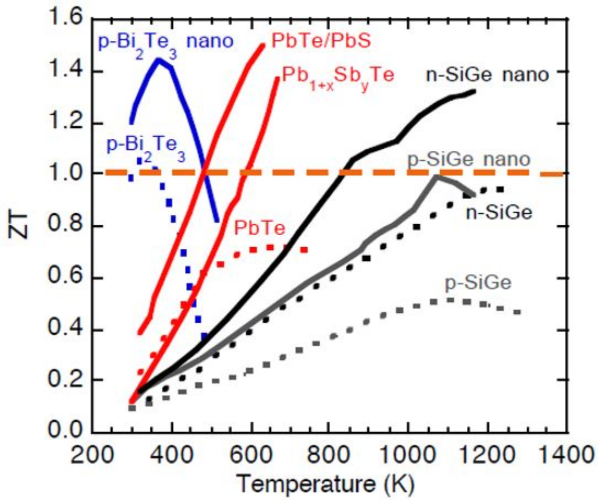

Figure 1.5: The figure-of-merit for conventional thermoelectric materials (dashed) and their nano-structured counterparts(solid)[4]

As seen from the expression of Eq. 1.10, a high ZT would entail a high Seebeck coefficient, high electrical conductivity and low thermal conductivity. However, there is a trade-off between these material properties. The Seebeck coefficient is higher in semi-conductors versus metals, and the opposite is true for electrical conductivity. Since the thermal conductivity is composed of both the lattice vibrations and the contribution from heat-carrying electrons (Wiedemann-Franz law), materials with high electrical conductance are usually good conductors of heat [4].

The ZT is used to calculate the efficiency which determines the thermal-to-electricity conversion.

$$\eta = \frac{T_1 - T_2}{T_1} \cdot \frac{\sqrt{1+ZT}-1}{\sqrt{1+ZT}+\frac{T_2}{T_1}} \tag{1.13}$$

The efficiency, as expected, is lower than the Carnot efficiency for an ideal heat engine as the term on the right of the multiplier that includes ZT is less than one. As

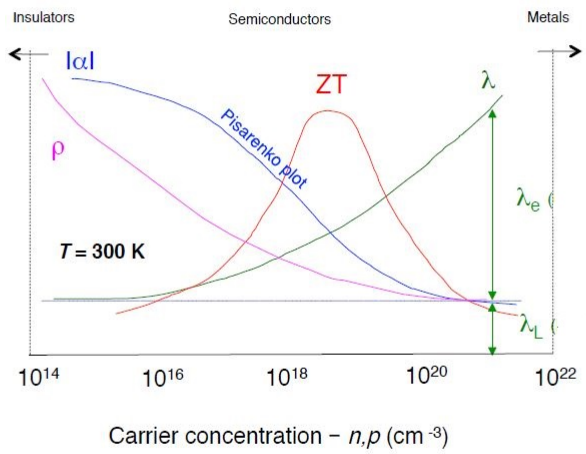

Figure 1.6: The relationship between properties as a function of carrier concentration [4]

shown in Figure 1.7, the efficiency increases with higher temperature difference between T_1 and T_2 and with higher ZT. Heat engines are usually around 30-40% efficient which would require a ZT of around 3-4 with ΔT$\approx 700K$ according to Figure 1.4. The highest ZT for bulk materials reported in literature was found to be about 2.2[36].

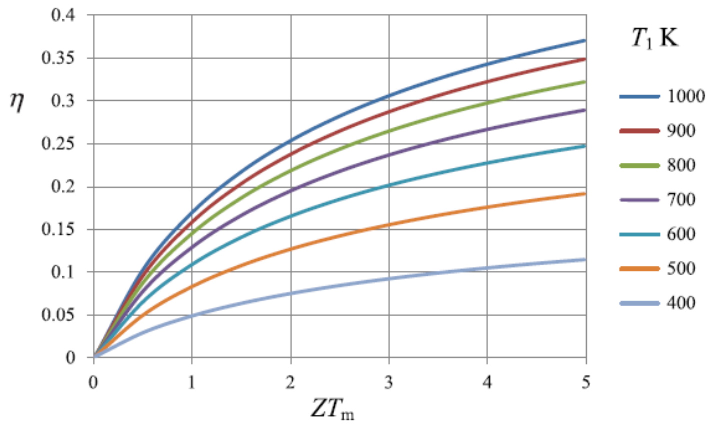

Figure 1.7: The efficiency as a function of the figure-of-merit and T_1, when T_2 is fixed at 300K [2]

The current state-of-the-art bulk thermoelectrics as n-type conductors are Bi_2Te_3, $PbTe$, $CoSb_3$, $SiGe$ and Sb_2Te_3, $PbTe$, $CoSb_3$, $SiGe$, $TAGS$ (Te-Ag-Ge-Sb) as p-type conductors [37]. Foreign atoms or native point defects can create local energy levels in the band gap. For example, a phosphorus atom that has 5 valence electrons in silicon, donates one to the crystal to fit the electronic structure of the host with four valence electrons. Phosphorous is a donor dopant in silicon and makes it an n-type conductor. A defect that can easily accept an extra electron from the crystal is an acceptor dopant, and thus is a p-type conductor. For example, a boron atom that has three valence electrons in silicon, accepts one from the crystal to again fit the electronic structure of the host. Thus, boron-doped silicon is a p-type conductor. [30]

An ideal thermoelectric material for generator applications was proposed by Slack and is based on a phonon-glass electron-crystal concept (PGEC). The idea is to obtain a material that has both low lattice thermal conductivity as in a glass and high electrical conductivity as in a crystal [38]. This can found in open and complex crystalline structures introduced with scattering centers for phonons such as impurities, dislocations or grain boundaries, all the while optimizing the charge carrier concentration to increase the power factor (numerator of the figure-of-merit) [2]. Clathrates and Skutterudites ($CoSb_3$) are both classes of materials that have crystalline cage-like structures that can host loosely bound impurities. They are particularly well-suited to form a basis for the PGEC concept. A promising but yet immature class of thermoelectric materials are metallic oxides. Although the figure-of-merit is currently far below than that of the state-of-the-art, these materials are stable both chemically and thermally from mid-to-high temperature ranges [33] and derived from elements that are abundant in nature.

Altogether, it is suggested to improve the performance of thermoelectric materials through primarily identifying and investigating new possible candidates which will be discussed in the final chapter. Through a combination of band gap engineering, alloying to form solid solutions and nano-structuring, enhanced thermoelectric properties can be achieved however one must consider both their interdependence within the figure-of-merit and dependence a function of temperature.

1.5 Thermoelectric modules

Thermoelectric modules (TEMs) are practical devices that are fabricated using thermoelectric materials with the purpose of converting significantly more heat into electricity. In such a device, n-type and p-type materials are connected electrically in series and thermally in parallel, and joined together by interconnects, all between two substrates as shown in Figure 1.8.

In general, if the TEM is very thick, the temperature gradient is large, which means

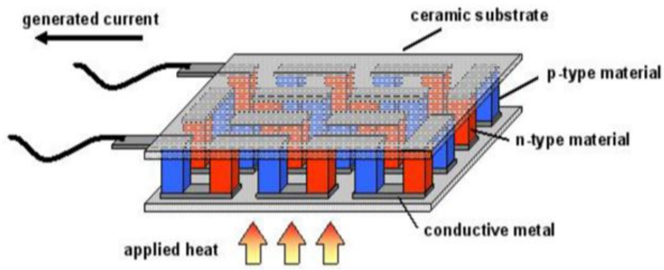

Figure 1.8: Schematic of a typical design and components of a thermoelectric module [5]

high electric potential, V, however the heat flux is small, which means small current, I. Since power is a product of voltage and current, there thus exists an optimal geometry to maximize power output given certain conditions [39].

However, even with the optimized geometry according to the temperature range and materials used, there are issues that reduce the performance of thermoelectric modules but some promising techniques/approaches to overcome them.

- One of most critical is the selection of interconnects and the binding of them to the n- and p- elements. The semi-conductor/metal junction exhibits a greater electrical resistance than a metal-metal junction, which greatly affects the performance of the device. Chemical diffusion due to concentration gradients also affect the electrical contact resistance. To avoid these issues, direct p-n junctions can be used or composite interconnects to decrease electrical contact resistance instead of using a metal/semi-conductor junction [40].

- Heat loss, especially thermal contact resistance is another major factor, which can significantly reduce the heat transfer through the device. Thermal contact resistance is caused by microscopic asperities which form irregular gaps between surfaces and depending how they interact from influences such as pressure and surface roughness, the thermal contact resistance can vary significantly. The use of thermal paste can be used to fill the micro-gaps and the choice of materials that are in contact play a role in reducing the thermal contact resistance [41].

- Thermal expansion also needs to be considered as mechanical stresses due to a mismatch between the n- and p- elements can lead to failure from crack initiation and propagation. A research group led by Professor Jeff Snyder at Northwestern

University have proposed a compatibility factor to match n and p-type materials for a suitable device as well as different materials within a leg in a segmented fashion [42].

With all these factors introduced that affect device performance, the actual efficiency is thus lower than the efficiency calculated with Equation 1.13. The actual device efficiency can be predicted via computational modeling techniques to include major factors. A strategic approach, that has been studied, is to calculate an effective figure-of-merit numerically using finite element techniques by taking into account temperature-dependent properties, the Thomson effect, thermal losses within the device (some of the results of this technique are shown in Figure 1.9) [6].

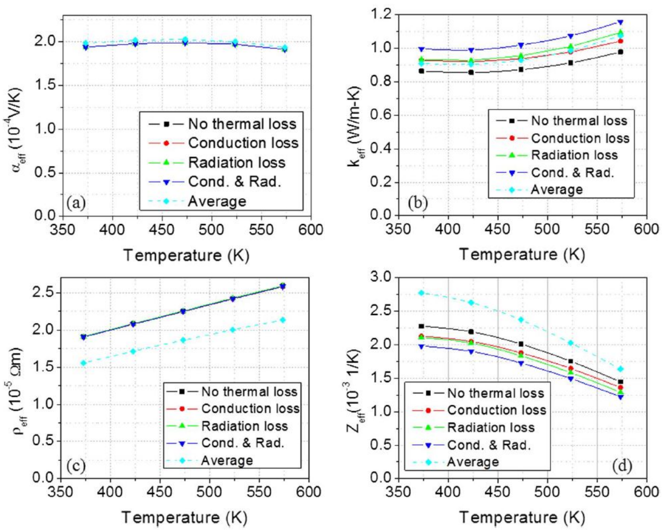

Figure 1.9: The calculation of the effective figure-of-merit by finite-element analysis including the effect of various factors [6]

One of the highest efficiency for a module (shown in Figure 1.10) that is not commercially-available but that has been recently presented as a main component of the next-generation TEG from the Jet Propulsion Laboratory (JPL) [43]. The TEM efficiency was reported to be 9.5% which corresponds to a ZT=0.68 for $T_h = 425°C$ and $T_c = 35°C$. As a comparison, one of the highest ZT reported in literature for this class of materials is 1.8 [44] which would corresponds to an efficiency of 17.8% for this temperature difference using Eq.1.13.

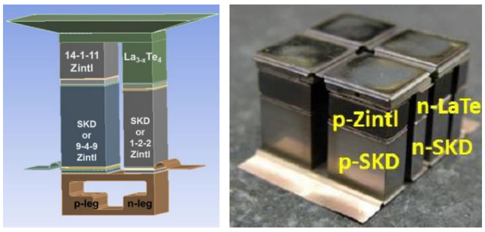

Figure 1.10: Left: Module concept by JPL[7]. Right: Proof-of-principle by JPL [7]

1.6 TEGs in a waste heat recovery scenario

A thermoelectric generator (TEG) is made up of three basic components: a heat source, thermoelectric modules (TEMs) and a heat sink. There is a cost associated to these components with TEMs being often the most costly. Cost-effectiveness is the main criteria in the terrestrial application of a TEG for power generation. Using waste heat as a source reduces the cost by eliminating the need for fuel. A TEG can be attractive for industrial applications such as power plants as a top-up cycle or a materials processing plant to its increase overall efficiency. Also, with the growing demand for power, there are also incentives from an investment standpoint to increase energy efficiency for existing industrial plants rather than investing in the capital infrastructure and operational cost needed for new plants as evidence from various rebate programs from governmental bodies or utility monopolies.

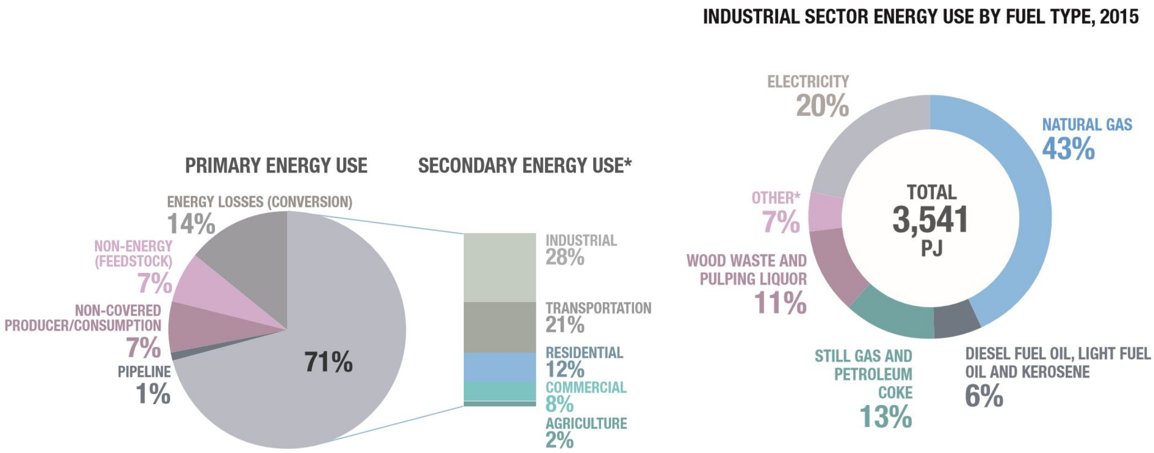

Figure 1.11: Left: Primary and secondary energy use by sector in Canada(2015)[8]
Right: Energy use by the industrial sector in Canada(2015)[8]

In 2015, Canada's industrial sector accounted for 28% of all the primary energy that is fed to secondary energy use that is for all final consumers in the economy[8] as shown on the left in Figure 1.11. In 2009, the amount of recoverable heat in liquid and gaseous streams from the industrial processes in Canada was estimated at 400 PJ/year [45]. Given that industrial energy use has increased by 31% from 1990-2015 [8], this amount of recoverable heat may be much more than what is previously stated. However given this amount still, using TEGs at a thermal-to-electricity conversion efficiency of 5-10% would reduce Canada's total industrial electricity demand from primary sources by roughly 3-6% (shown on the right in Figure 1.11).

However, for an economically viable scenario, the cost per unit power produced or purchased should be lower than the combined capital and operational cost per unit of power produced by the TEG. Other potential technologies such as the heat recovery steam generator, organic Rankine cycle or reciprocal engine are theoretically more efficient, however due to their size and complexity, there can be practical issues in the case of a retrofit and the requirement of specific inputs or conditions to function continuously. There are also other heat recovery solutions through the use of heat exchangers or refrigeration via compression cycles to manage streams and make use of excess heat for other plant needs which can be a cheaper option to implement and maintain. However, with various possible solutions for stakeholders, a decision-support tool would be a useful approach to provide industry with options to compare the benefits for their specific cases[46].

There are advantages in using a TEG as a retrofit to recover an existing plants' waste heat and it should be an option in a potential decision-support software as the technology emerges. It can have a relatively simple design being completely passive with no moving parts, and highly reliable from evidence of those working for over 8000 hours with little maintenance [23]. To design and implement a cost-effective generator and competitive solution, however, an entire system approach is required. This includes the production of low-cost material and modules with high ZT throughout the applications' temperature range as well as the optimal coupling of heat exchangers with modules to maximize power output and minimize cost. The optimized electrical connection of the modules and as well as conditioning the power output of the modules to a corresponding load or storage device also are aspects to consider.[47]

The scope of this work is focused on the coupling of heat exchangers and thermoelectric modules to capture, concentrate and convert waste heat into electricity and further prove the concept of a scalable and modular thermoelectric generator design for industrial applications.

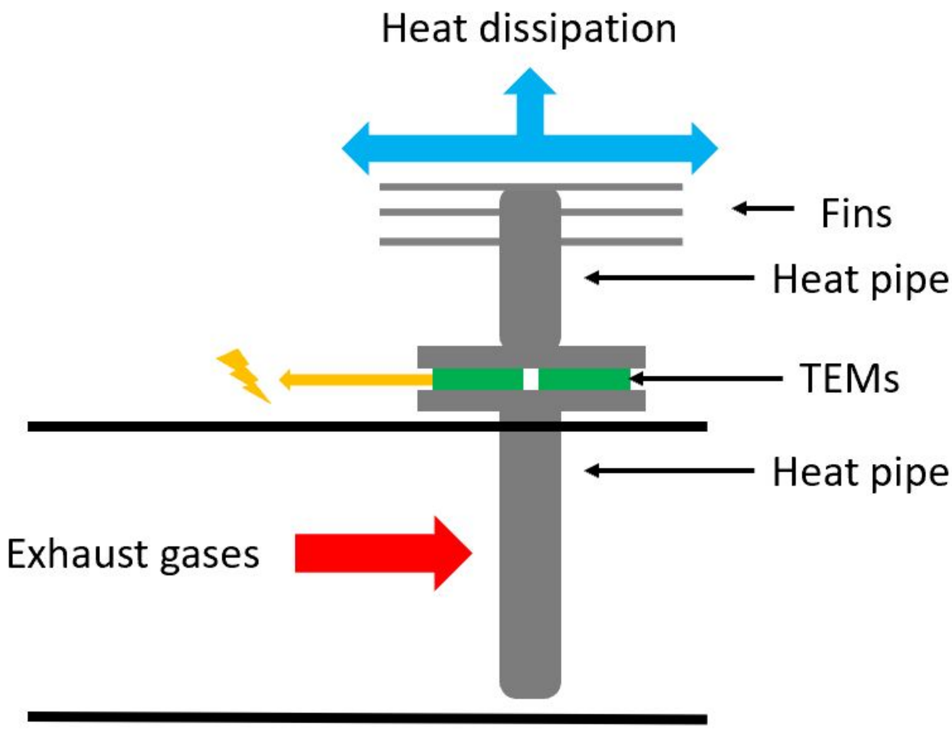

Figure 1.12: Schematic of the modular TEG design

As described in Figure 1.12, heat pipes are chosen as the heat exchanger to capture and concentrate the waste heat. They can have a heat-transfer capacity of several orders of magnitude higher than solid conductors such as copper or gold [48]. Also, the evaporator and condenser can be separate and of different geometries, hence a concentration of heat at the condenser can provide greater heat flux which can produce more power per area of TEMs, potentially lowering costs of most expensive component. The use of heat pipes can also effectively dissipate the rest of heat and have been found to produce more power for a TEG versus other conventional heat exchangers. The topic of the next chapter is a brief review of the recently published work done on the coupling of heat pipes and TEMs to form a TEG for waste heat recovery applications.

Chapter 2

Literature Review

A TEG prototype was built for waste heat applications Remeli et al.[9]. The TEG consists of finned heat pipes to both capture and dissipate the waste heat with thermoelectric modules placed in between using thermal spreaders. Although not depicted in Fig.2.1, they used a U-shaped duct which at one end, ambient air is forced to cool the cold-side finned heat pipes which is subsequently heated to provide hot air to the hold-side finned heat pipes. The TEG consists of 8 units, with each unit comprising of four copper/water heat pipes with 62 aluminum fins on either side and 6 TEMs (40x40mm each) connected electrically in series as shown in Figure 2.1.

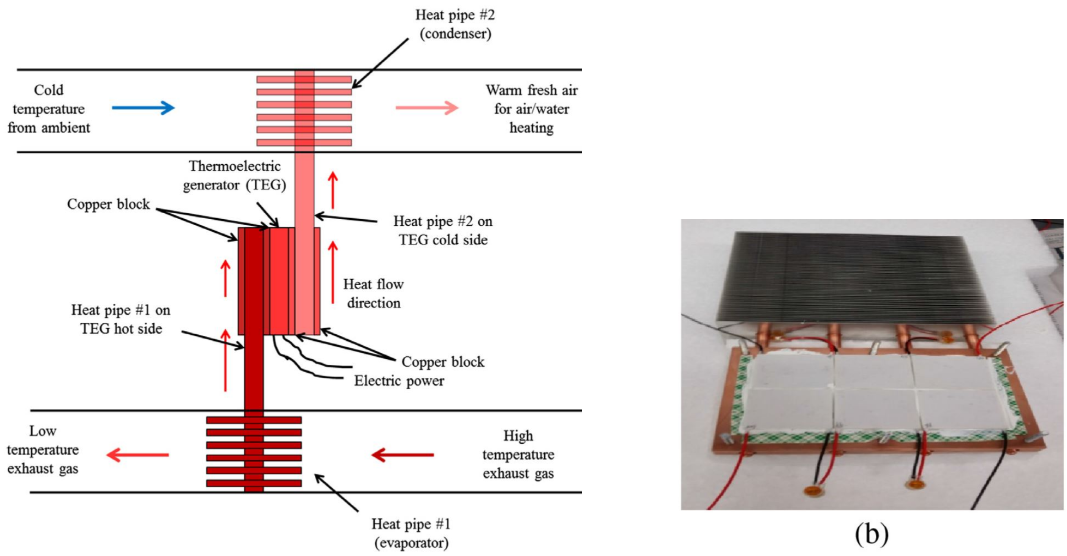

Figure 2.1: Left: TEG concept. Right: One unit of the build TEG excluding one side of heat pipes.[9]

At an air velocity of 1.1 m/s, the first unit encountered by the flow of hot air reaches a power output of approximately 1.3W, and decreases slightly for each subsequent unit for a total maximum power output of 7W. The heat transfer rate was calculated using the effectiveness of the heat exchanger, the temperature measurements of both cold air inlet/outlet and hot air inlet/outlet and the mass flow rate. The efficiency of the TEG was calculated to be 0.65% was obtained with $T_h \approx$ 105°C and ΔT$\approx$ 30°C.

The work by Orr et al.[49] uses the same concept but to recover the waste heat from car engine exhausts. A working prototype was built and tested, using 8 TEMs (62mm x 62mm each) and copper/water finned heat pipes on each side as shown in Figure 2.2. The maximum power generated was found to be approximately 38W with a resulting efficiency of 2.46%. This was achieved with $T_h \approx$ 200°C and ΔT$\approx$ 105°C.They also varied the orientation of the TEG, with three different positions according to the waste heat flow. They found that when the exhaust was located at the bottom (Figure 2.2), a higher power output was achieved than having it on top and placed horizontally.

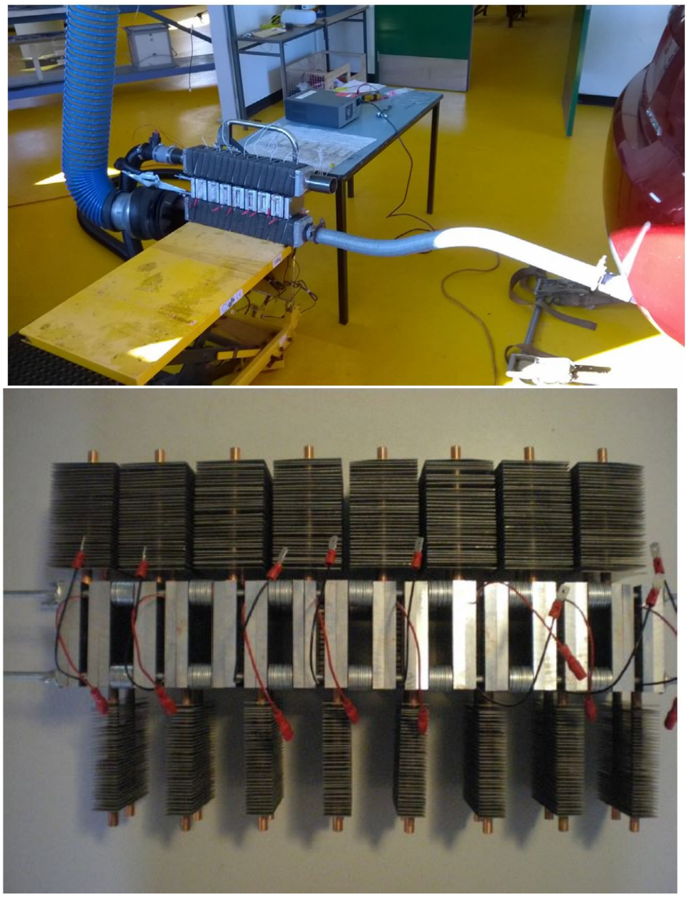

Figure 2.2: Top: TEG prototype connected to car exhaust. Bottom: TEG close-up

Aranguren et al.[50] did a computational analysis to compare the effect of the heat sink on power output of a TEG. They concluded that using heat pipes significantly increased power output versus a finned heat sink, even by 13% when using optimal fin spacing. Araiz et al.[51] followed this work through experiment using thermosyphons, which are essentially wickless heat pipes, as heat sinks to dissipate heat on the cold-side of TEMs as shown on the left in Figure 2.3. They used statistical analysis on the performance of TEG using a thermal resistance network as a model to determine the influence of key parameters of cold-side heat exchanger. In doing so, the prototype design was optimized which resulted in 36% more net electrical power compared to a finned heat sink with a fan.

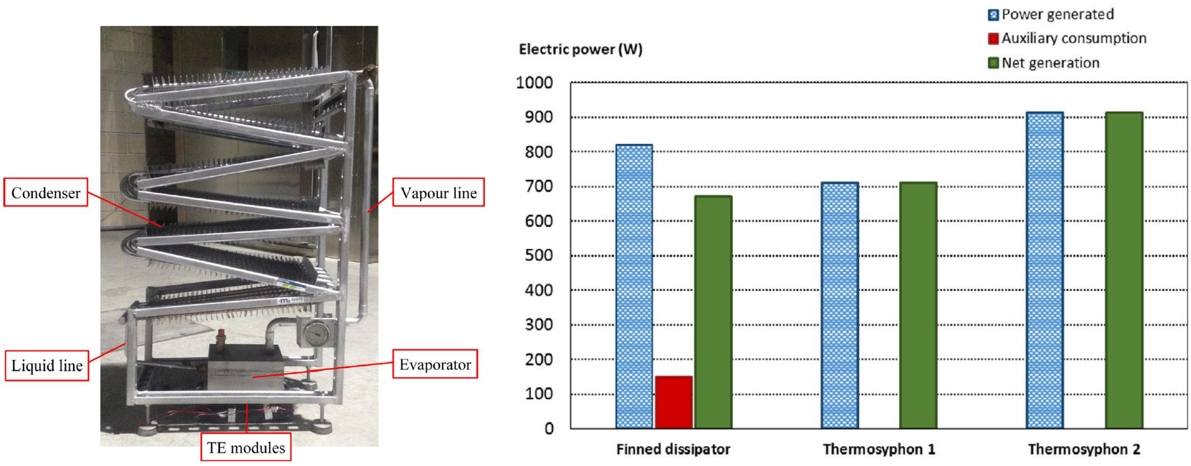

Figure 2.3: Left: TEG prototype with a thermosyphon, a wickless heat pipe working with gravity. Right: Power output comparison for different heat sinks

Aranguren et al.[52] further proves the importance of eliminating auxiliary power from the heat sink system on an industrial-scale application. They do so by using a more detailed computational model with a finite-difference approach and compare the passive heat pipe system to a refrigeration based-system. They found that the TEG can produce a maximum of 119 MWh/year for a given furnace working 350 days/year using the refrigeration based-system as the cold-side heat exchanger. However, the net generation is reduced by 40% due to the auxiliary consumption of the pumps and fan-coil required for the refrigeration based-system. They also suggest a scenario to eliminate the fan-coil by having a water reservoir nearby, which can lead to a net generation of 121 MWh/year. On the other hand, using a passive system, as the one described [51], they calculate a net generation of 128 MWh/year, 75% higher than the refrigeration-based system.

Lv et al.[53] studied through experimental testing, the cost-performance of three different cooling systems for TEGs: air-cooled fins, water cooling exchanger and a heat pipe based exchanger. For each case, forced convection by a fan through a enclosed channel encompassing the fins as shown on the top of Figure 2.4. Although net power was found to be higher for the heat-pipe based cooling system, there is still auxiliary power used for forced convection which was the most for this system. According to their set-up, there is more work done to maintain the air flow as the pressure drop across the fins is larger for the heat-pipe system. However, the authors state that natural convection can also be used instead with larger fins to also dissipate heat efficiently with less auxiliary consumption. They also compared the experimental results with models based on a thermal resistance network for the heat exchangers, and a simplified model similar to the one found in [34] for the TEM. They found good agreement between the model and the experimental results, with a maximum difference of less than 5%.

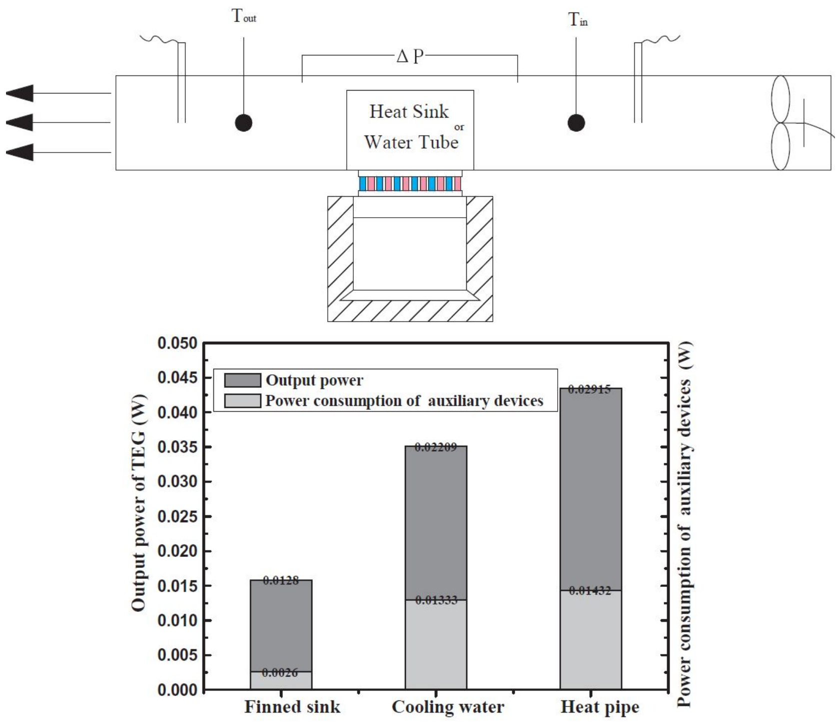

Figure 2.4: Top: Schematic of TEG set-up Bottom: Net power output comparison of the cooling systems

They define the heat exchanger cost in $USD per unit Watt and of temperature. Although, the heat pipe system has a higher capital cost, it is calculated to be $\frac{\$10.67}{W \cdot K}$ versus $\frac{\$13.81}{W \cdot K}$ and $\frac{\$15.12}{W \cdot K}$ for the air-cooled and the water-cooled heat exchanger respectively.

Chapter 3

The TEG development

3.1 Prototype design

A bench-top prototype was designed (as shown in Figure 3.1) and built (as shown in Figure 3.9) as a proof-of-concept for recycling waste heat into electricity with a TEG.

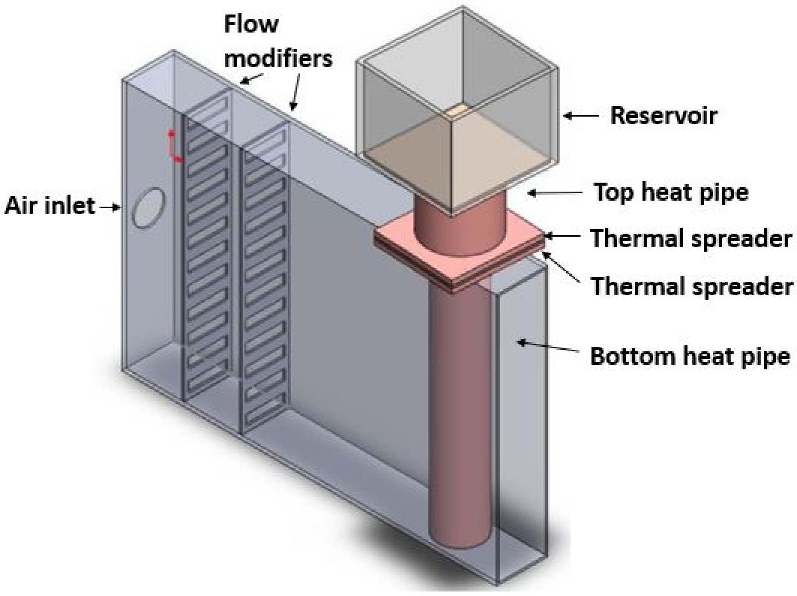

Figure 3.1: Conceptual design of the TEG prototype [10]

The role of the duct is to contain and conduct the flow of hot air, an inlet was designed to place the source of waste heat. To ensure the uniform distribution of air throughout the cross-section, two flow modifiers are used at specific distances from the inlet. This configuration has been found to have the best outcome compared to difference designs and placement locations [10]. This was later confirmed using ANSYS® Fluent as shown in Figures 3.2 and 3.3, the difference of the fluid flow behaviour using one flow modifier versus the use of two. The numerical procedure in section 3.5.3 and the mesh sensitivity analysis can be found in 5.12 Appendix for the two flow modifier design.

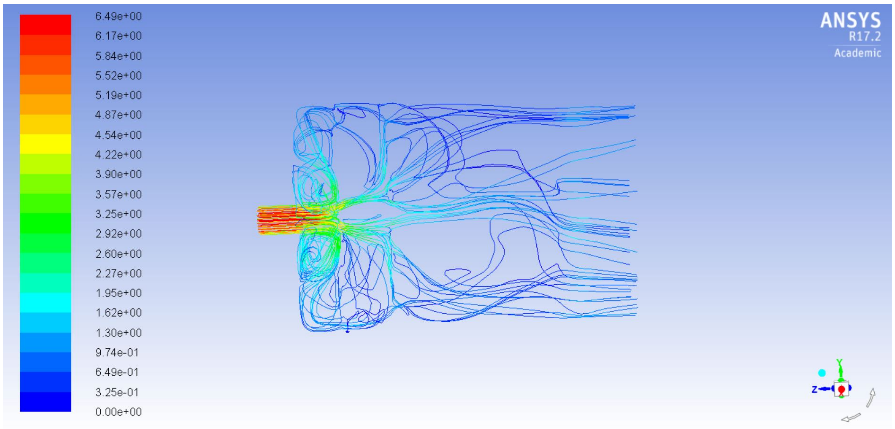

Figure 3.2: The effect of the two flow modifiers on the fluid flow in the system

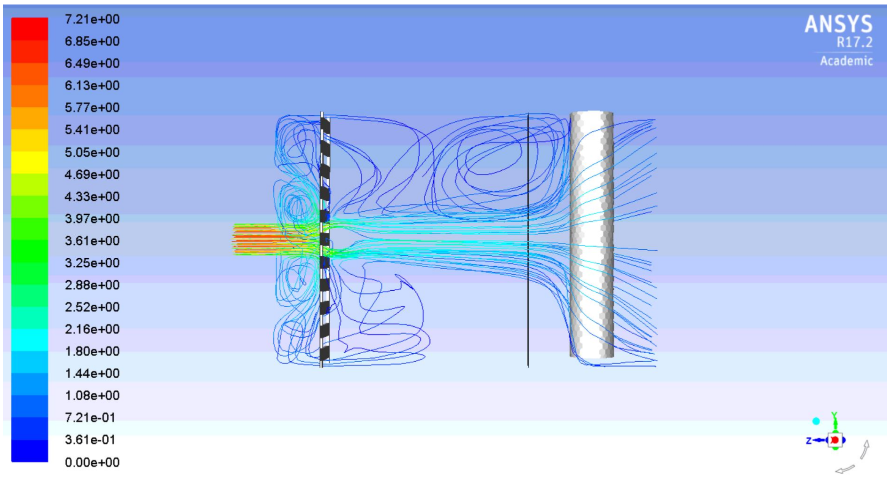

Figure 3.3: The effect of removing the second flow modifier

The bottom heat pipe serves as a heat exchanger to transfer heat from the hot air to the bottom thermal spreader which leads to the "hot-side" of the thermoelectric modules (TEMs). The top heat pipe also serves as another heat exchanger to transfer heat from the "cold-side" of the TEMs through the top thermal spreader to the sink which is a reservoir on top. Although not depicted in Figure 3.1, the thermoelectric modules are placed between the top and bottom thermal spreaders which experience a temperature gradient across them and thus can generate an electric potential via the Seebeck effect.

3.2 Design methodology

The objectives in the design phase were the following:

- To be portable and fit on a bench-top
- To demonstrate functionality by powering a device continuously

These criteria were framed around a real-life waste heat recovery scenario and so, a duct and a source of heat was needed to conduct the flow of hot gases. A rectangular duct was fitting as it could be easily fabricated to encase a single heat pipe. This would therefore encompass the modular aspect for industrial applications for which an array of heat pipes could be used to capture and concentrate a large amount of heat. The prototype was thus designed to act as one pipe in an array. As for the source of heat, it needed to be continuous but also temperature-controlled for testing purposes. A variable-temperature heat gun typically used for drying in paint applications met the necessary criteria for a source of heat, and the flow rate could be varied to two different settings, which would become another parameter to test. Since the diameter of the heat guns available would be significantly smaller than the desired cross-sectional area of the duct, it was deemed that the hot air stream would be concentrated at a specific area. The problem was then to ensure the air in the duct would have a relatively constant velocity throughout its cross-section to better emulate a waste heat stream and therefore what the heat pipe would be experiencing in a real-life application. The use of flow modifiers which are essentially obstructions in the flow, were engineered in this case to straighten the flow for a constant velocity at a set plane in the cross-section just before reaching the heat pipe, which would be deemed as the bulk velocity. As described previously, different designs and configurations of flow modifiers were tested and simulated in another work, and the best outcome came when using two perforated plates with rectangular slits, as seen in Figure 3.1, at specific distances from the inlet (see Appendix)[10].

The sizes for all the components were chosen based on the first design criteria, and exact dimensions adjusted based on the availability from suppliers. The choice of material for the duct was aluminium based on its low weight, cost as well as its thermal properties compared to other available materials.

As for the selection of materials and design of the heat pipe components, this would be crucial in meeting the second criteria. First, although it may be attractive economically to use a steel alloy as an envelope, this combination has been shown to be incompatible with water as a working substance as it can react to form a non-condensable hydrogen gas according to the equation below[54].

$$Fe + 2H_2O(l) \rightarrow Fe(OH)_2 + H_2(g) \tag{3.1}$$

The hydrogen gas would create an additional thermal resistance and decrease the heat transfer to the TEMs. This can be avoided by manufacturing a passive layer or coating on the inside surface of the pipe and/or using an inhibitor to minimize oxidation, however this adds an unnecessary level of complexity in terms of the purpose of the bench-top prototype. Although, the generated gas could be purged over time, the heat pipe would not meet the requirement of continuous operation. To avoid such issues, a proven combination of copper as an envelope and water as a working substance was used.[54]

The choices for the diameter of the copper pipe from the supplier were approximately 1,2 or 3 inches. There was a trade-off to consider as both the heat captured by the pipe and the heat transported axially would increase with increasing diameter.

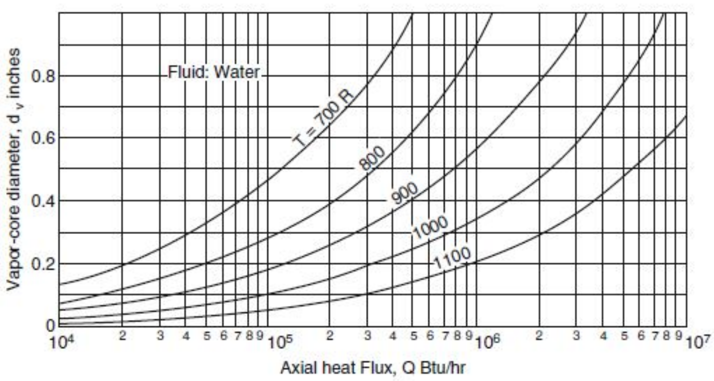

Figure 3.4: Vapor core diameter versus heat transfer rate for vapor Mach Number of 0.2 for water(Inch=0.0254m, 1Btu/h= 0.2929W, 1R=0.5556K)[11]

However, an increased diameter can possibly lead to a compressed vapor flow which leads to a large axial temperature gradient, decreasing the effective thermal conductivity and thus performance of the heat pipe. The 2 inch diameter pipe was chosen for the bottom heat pipe and the 3 inch diameter pipe was chosen for the top heat pipe. With a decreased vapor temperature in the top heat pipe, it is less likely to reach a compressed flow, and so the larger diameter was chosen as a significant increase in area and vapor-core diameter would allow more heat to be transported from the cold-side of the thermoelectric modules. [12]

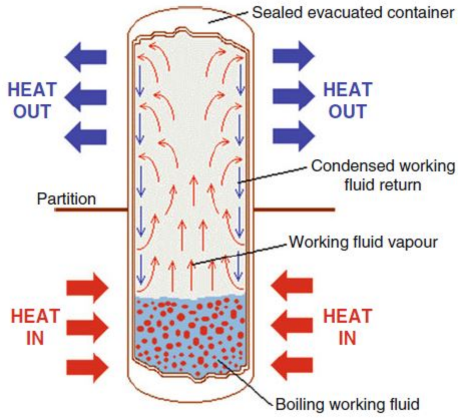

Figure 3.5: Schematic of the working principle of a heat pipe[12]

In order for the heat pipe to perform continuously, it is vital to ensure enough working fluid returns to the evaporator section after the release of its heat in the condenser so that the cycle can repeat without reaching a dry out limit. The transport phenomena being described as the return of liquid is governed by surface tension. It naturally causes a pressure drop by pulling a liquid at a solid interface which contributes to a contact angle that forms a meniscus as equilibrium is reached. The effect of vaporization and condensation causes a varied curvature of the menisci along the length of the heat pipe (as shown in Figure 3.1) which ultimately contributes to the vapor-liquid pressure difference in both regions. A capillary structure such as wick is commonly used on the inside of the pipe to enhance this effect and essentially provide the necessary driving force by maintaining a net pressure difference between the evaporator and condenser.[34]

There exists different wick structures and the choice depends on the working substance among other factors [54]. For sake of simplicity in the assembly, cost-effectiveness of manufacturing and recommended past use, a mesh screen was chosen. The mesh size is the main design parameters to consider when using this structure. The mesh size or mesh

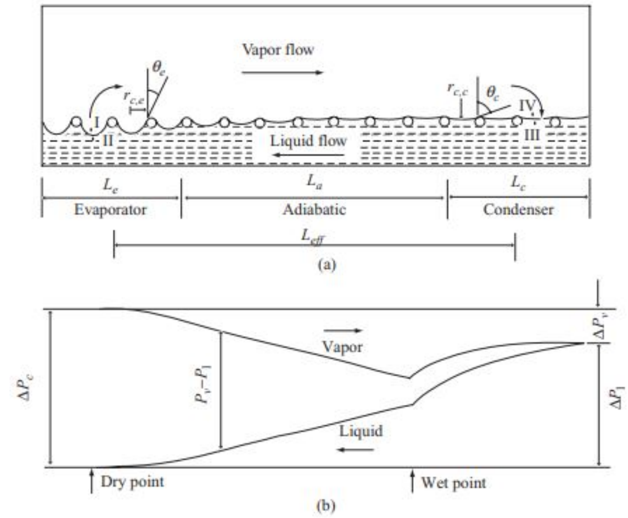

Figure 3.6: Top: Variation of meniscus curvature as a function of axial length. Bottom: Typical liquid and vapor pressure distributions in a heat pipe[13]

number has an effect on the capillary pressure and permeability. As the mesh number increases, the capillary pressure increases however the permeability decreases. With a decrease in permeability, there is a increase in pressure drop due to the increase in resistance to the liquid flow and the heat transport limit shifts downwards. However, the effect of permeability has less of an impact in shorter heat pipes, as the trade-off for an increase in capillary pumping pressure is more beneficial for heat transport. A greater mesh size number could therefore be used for the prototype as length was limited by the first design criteria.[12]

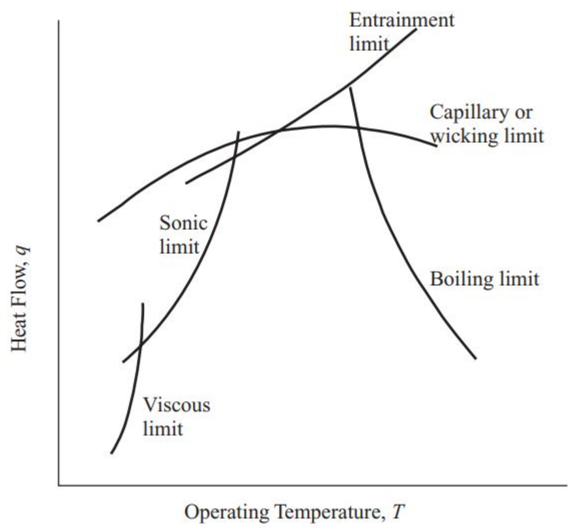

Figure 3.7: Schematic of heat transfer limitations on heat pipe performance[13]

Furthermore, it is critical to consider the effect of boiling on the continuous operation of a heat pipe especially at higher operating temperature ranges. The radial heat flux through a surface varies with a temperature difference between the wall of the pipe and the temperature of the working fluid as seen in Figure 3.8 below. As the radial heat fluxes increase, there is an increase in bubble formation as seen in Figure 3.8 between point B and C. The rate of heat transfer increases to a maximum (point C) until the amount of bubbles increase so high that a insulating layer of vapor forms at the inner surface of the heat pipe (point C to D). This is known as the boiling limitation. Although, high heat fluxes are not expected to occur due to the relatively low grade stream of hot air, it is still important to consider as it can lead to failure through overheating. The use of a flow modifier in the evaporator section of the heat pipe can overcome this boiling limitation. The flow modifier can have many different designs with its dual function being to use centrifugal force to push the vapor bubbles from the wall and to continuously provide a uniform layer of working substance at inside walls of the heat pipe. This design could ultimately allow more heat to be captured and thus transferred to the thermoelectric modules at the condenser. [55, 14]

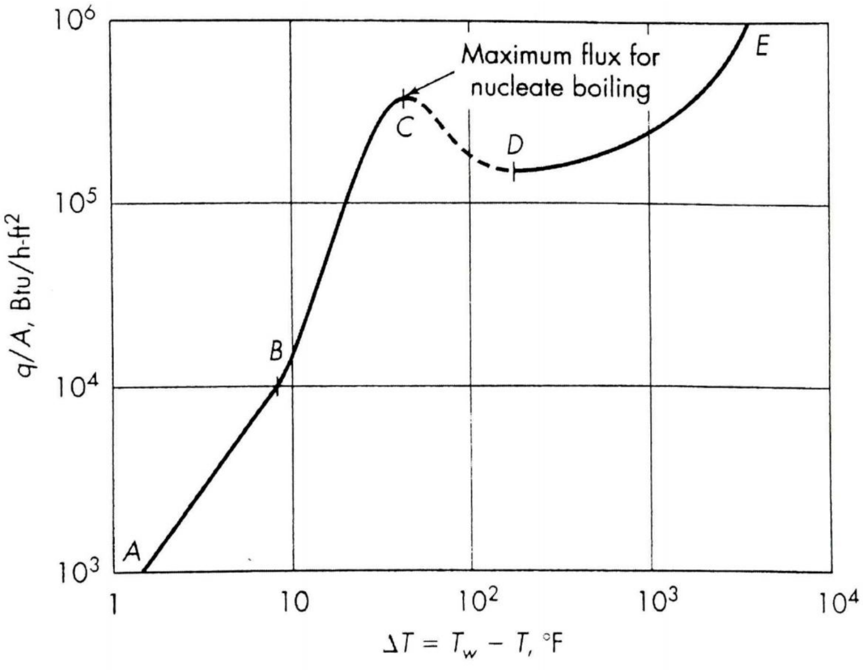

Figure 3.8: Pool boiling regime; heat flux versus temperature drop (water boiling at 1 atm) [14]

Although water as working substance in heat pipes can operate from 30°C to 200°C ([54]), it is recommended to work below this to avoid reaching its heat transfer limitations and ensure continuous operation [14]. In selecting the thermoelectric modules (TEMs), the rated hot-side temperature is a very important factor to consider. According to the preliminary design, it was assumed that the working temperature of the heat pipe would be approximately the hot-side temperature of the thermoelectric modules with minimal thermal resistance between these two components. The temperature at the hot-side of the module was thus estimated to be below 200C° according to the operating range of a copper-water heat pipe. Therefore, a bismuth telluride(Bi_2Te_3)-based TEM was the best choice in terms of performance. According to specifications from a manufacturer, a TEM with a hot-side temperature of 200C° and cold-side temperature of 30°C, would be able to output a maximum of 3W at matched load[56]. The material selection for the thermal spreaders was based on its compatibility to bond with the heat pipe to ensure proper enclosure of it. Using copper was a good choice as joining similar metals is preferable, and given the high thermal conductivity of copper, the temperature between the hot-side of the modules and the bottom heat pipe would be minimized by reducing the thermal resistance along the path of heat. Furthermore, given that the thermal conductivity of copper is isotropic, transferring the heat to larger surface area was deemed to have a small temperature drop from a thermal resistance due to spreading. Therefore, an increase in the number of TEMs would increase the power output given that the temperature gradient could be maintained. The thermal spreaders were thus sized to host four TEMs to maximize power.

The final component to be designed was the reservoir, and using the same methodology for the thermal spreaders, a copper plate would be joined to the at the top of cold-side heat pipe, to effectively reject the heat from the condenser to the sink. Although, a water-ice bath would perform better as a heat sink in the top reservoir, a water-dry ice combination was used instead for convenience purposes due to the lack of refrigeration available in the testing area.

3.3 Prototype assembly

The duct and the flow modifiers were machined and welded from sheets made of aluminium to specifications that can be found in the Appendix (as shown in Figure 3.9).

Figure 3.9: The fabrication of the duct and placement

Both heat pipes have copper envelopes and use water as a working substance, as mentioned, an adequate combination due to compatibility [57]. A stainless steel mesh was point welded around the inside wall of the envelopes to serve as a wick. The wick was placed between the inside wall and a stainless steel spring for the bottom heat pipe. The purpose of the spring (shown in Figure 3.10) is to induce a swirling effect which propels liquid against the inner walls using centrifugal force [58]. Although a spring was used both on the top and bottom of the bottom heat pipe, this was to maintain the wick in place. As for the top heat pipe, retainer rings were used instead for this purpose.

Figure 3.10: The inside at the top of the bottom heat pipe

A copper plate was soldered to the open top of the pipe to serve as the thermal spreader and a copper cap was soldered to the open bottom of the pipe. A hole was drilled to place and to solder a quarter inch copper tube at the top of the pipe and just below the thermal spreader. This serves two purposes, one is to inject the water into the pipe and the other is to create a vacuum above the water level by removing air using a pump and a shut-off valve. A similar procedure was used to build the top heat pipe. The difference is that the thermal spreader is soldered to the bottom of the top heat pipe and a thinner copper plate soldered to the top of it. The copper plate was contained with four walls made of PMMA (plexiglass) surrounding it to form a reservoir with an open top. A The purpose of which was to maintain a temperature of the bath to serve as a heat sink with a boundary condition for experimental tests and modeling. Next, four holes were drilled at the corners of each of the thermal spreaders to insert bolts which can connect the bottom section to the top section and press them together using wingnuts. Four thermoelectric modules were then connected in series and placed in between the top and bottom thermal spreaders to finalize the thermoelectric generator assembly. In order to function, a variable temperature heat gun is used as a heat source and the positive and negative terminals of the TEMs are connected to a load to use the electricity generated as shown in Figure 3.11.

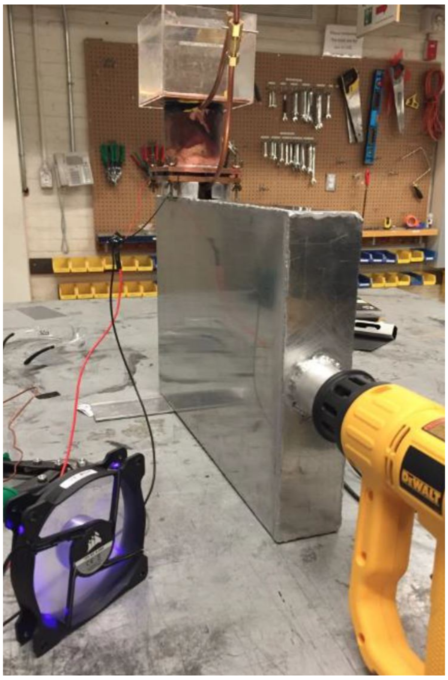

Figure 3.11: The assembled prototype powering a computer fan

3.4 Experimental set-up

The next goal was to measure the power output of the TEG as a function of the inlet temperature and flow rate from the heat gun. The four modules, connected in series, were connected to the load (a computer fan - see Appendix for specifications) and a current sensor (INA 219 - see Appendix for specifications). Through I2C software communication, a Raspberry Pi 3 computer can transmit data of the voltage across a shunt resistor as shown in the schematic in Figure 3.12. Four type K thermocouples (TCs) were placed at key locations (bottom and top heat pipe, bottom and top thermal spreader) using thermally conductive epoxy under a layer of epoxy to hold them in place and ensure the conduction of heat through the thermocouple tip to avoid heat loss. The thermocouples were connected to a data acquisition device NI-9225 from National Instrument™ for continuous temperature measurements using the data acquisition add-on from MathWorks®.

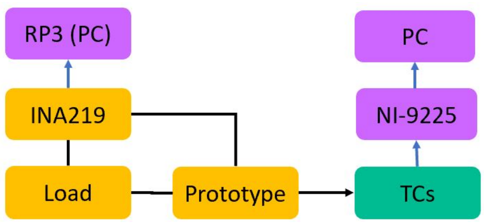

Figure 3.12: A schematic of the experimental set-up and the flow of data acquisition

According to the maximum power transfer theorem, the maximum power delivered to a load is when the resistance of the load would be equal to the internal resistance of the modules. However, it has been determined that for a thermoelectric generator the ratio between the load and internal resistance is actually about 1.4 to achieve maximum power transfer[39]. The load has a rated voltage of 7V to 12V and rated amperage of 0.26A, the resistance should thus vary according to voltage across the load from around 27Ω to 46Ω. The internal resistance of each module from data provided by the manufacturer increases linearly as function of hot-side temperature. At an estimated value of around 5Ω, using four modules in series, the internal resistance of the TEG would be 20Ω. Using the ideal ratio mentioned earlier, the maximum power transferred would be at matched load of 28Ω, which is in the range of the computer fan's internal resistance.

The top box was filled with a mixture of dry ice and water and maintained at roughly 5°C (±2) manually by adding/mixing dry ice and monitoring the temperature using a handheld thermocouple. The inlet temperature of the gun was set to 500F(260°C) for the first test and increased by 100F($\approx$ 56°C) to 1100F ($\approx$ 593°C) for subsequent tests. The volume of water used in the heat pipes was determined by calculating the equivalent amount water for a 2mm film for the entire inner surface area of the heat pipes. For the bottom heat pipe and top heat pipe, a total of 135ml of water and 36ml of water was used respectively. To purge the system, a handheld vacuum pump (see specifications in Appendix) was used until manually possible and the valve shut. A pressure gauge was placed between the purging tube and the valve to ensure the vacuum was maintained. Figure 3.13 shows the experimental set-up during a test run.

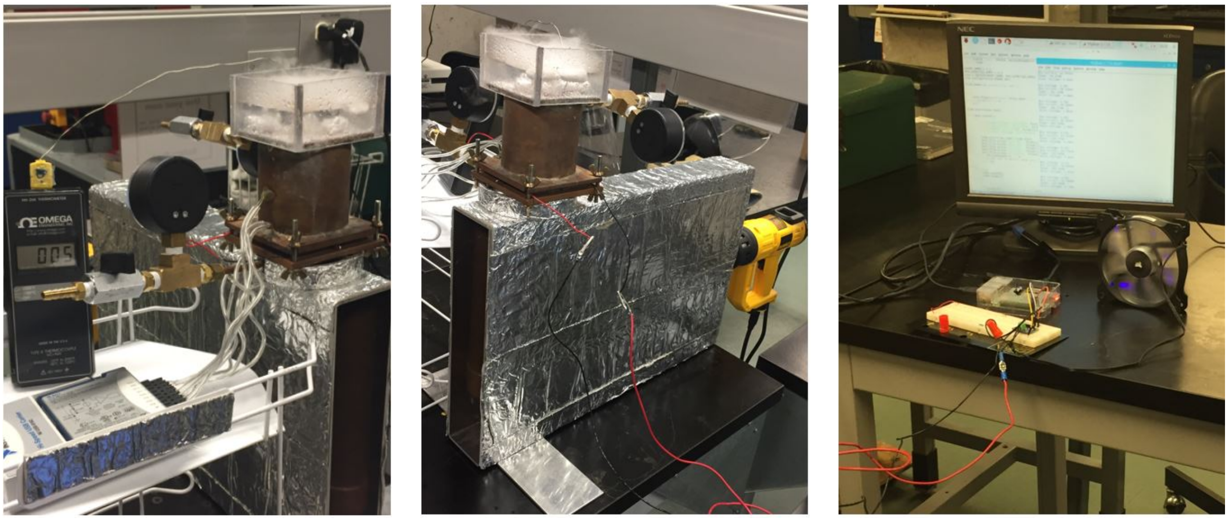

Figure 3.13: Pictures of the experimental set-up during a test run

3.5 Modeling techniques

In order to predict the power output of the TEG and then compare this to the experimental results, two models were used: a simplified [34] and detailed one from [15]. Both models are provided with the hot-side temperature, T_h, and the cold-side temperature, T_c acquired from the experimental data along with the material properties of the TEM. Since the theoretical power output increases linearly with increasing number of thermocouples, the result from one n- and p-leg combination is found and multiplied by the number of couples in the TEG. A description of each model used will follow.

3.5.1 Simplified TEM model

The model assumptions:

- 1-D, steady-state
- No heat loss
- TE properties are evaluated at the average between the hot and cold-side temperature
- The heat absorbed at the hot junctions is equal to the heat supplied at the source
- The heat released at the cold junction is equal to the heat rejected to the heat sink

The simplified TEM model is described by a heat balance within a control volume of one of the legs by applying conservation of energy. The heat balance considers the conduction by Fourier's law and Joule heating [34].

$$Q_{in} - Q_{out} + Q_j = 0 \tag{3.2}$$

At the hot junction for the p-leg, the expression is derived to the following:

$$Q_{ph}(0) = (\frac{\kappa_p A_p}{L_p})(T_h - T_c) - \frac{0.5 I^2 \rho_p L_p}{A_p} \tag{3.3}$$

The expression is expanded to include the Peltier effect.

$$Q_{ph}(0) = -\alpha I T_h + (\frac{\kappa_p A_p}{L_p})(T_h - T_c) - \frac{0.5 I^2 \rho_p L_p}{A_p} \tag{3.4}$$

The total heat in at the hot-junction is thus the sum of the heat entering the n and p-leg.

$$Q_H = Q_{ph} + Q_{nh} \tag{3.5}$$

The same applies to find the expression for total heat out at the cold-junction. The power output is the difference between the total heat out and the total heat in. The optimal current can be found by differentiating this expression with respect to current. The total maximum power output for each thermoelectric module is therefore this multiplied by the number of couples.

$$P_{max} = Q_H - Q_C = N \cdot (\alpha_{pn} I_{opt}(T_h - T_c) - R_{pn} I_{opt}^2) \tag{3.6}$$

$$I_{opt} = \frac{\alpha_{pn}(T_h - T_c)}{2R_{pn}} \tag{3.7}$$

3.5.2 Detailed TEM model

The model assumptions:

- 1-D, steady-state
- Heat loss due to conduction and radiation in the air gaps between legs
- Temperature-dependant TE properties
- Thomson heating is considered, which is the heat absorbed or released depending on the direction of the current
- Thermal resistance of the substrate and interconnects are considered
- Electrical resistance of the interconnects are considered

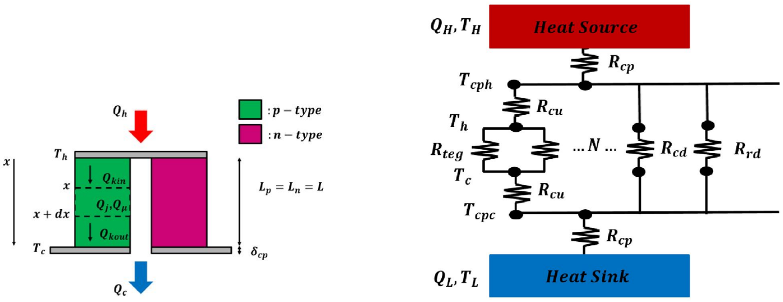

Figure 3.14: Left: A schematic of the detailed model. Right: A schematic of the thermal resistance network [15]

A 1-D heat balance of a control volume within a leg (as shown on the left of Figure 5.3) is used to derive the governing equation by Taylor expansion.

$$Q_{in} - Q_{out} + Q_j + Q_\mu = 0 \tag{3.8}$$

$$Q(x) - Q(x + dx) + Q_j + Q_\mu = 0 \tag{3.9}$$

For the p-leg:

$$Q(x) - (Q(x) + \frac{dQ(x)}{dx}dx + \frac{I^2 \rho_p(T_p(x))}{A_p}dx - \mu_p(T_p(x))IdTp(x) = 0 \tag{3.10}$$

Since temperature is a function of position, and the properties are a function of temperature, the model cannot be solved analytically. In Matlab, a boundary-value problem solver (bvp4c) is used to numerically solve a set of first-order ordinary differential equations [15]. An initialization is first done by providing a 1-D mesh for each leg along with an initial guess for each point. The temperature-dependant properties are described as a polynomial using Matlab's polyfit function from the manufacturer's data [59]. The other inputs include the hot-side and cold-side temperature which was determined experimentally as the deemed steady-state temperature. The thermal resistances of the interconnect, substrate which includes both the ceramic and graphite portion and the electrical resistance of interconnect were calculated using a thermal resistance network based on the manufacturer's specifications. The heat loss due to radiation is considered from the ceramic on the hot-side to the ceramic of the cold-side. The equations for thermal and electrical resistance and the data from the manufacturer are presented in the appendix. The set of equations and their respective boundary conditions are solved within a thermal resistance network as shown on the right of Figure 5.3. A tolerance is set within the solver, the initial guess starts the iteration process until the residual of each equation reach this tolerance. During the process, the current, I, is recomputed as the heat absorbed and rejected at the junctions change during the iterations. Once the solution is converged, the temperature profile along the legs is obtained. The output power is calculated based on the final value of I and the difference between the final computed values of heat absorbed and rejected. This is the power output for one couple and the total output is proportional to the total number of couples in the system.

3.5.3 Heat captured by the TEG

In order to determine the heat captured by the bottom heat pipe, the temperature of the pipe wall and air flowing past the pipe as well as the velocity should be known. Using these values, an empirical relation for a cylinder in a cross flow can be used to calculate the heat captured by the TEG. In this case, the temperature of the pipe wall can be estimated with the experimental values obtained from a thermocouple located on the bottom heat pipe, assuming the exposed surface area of the pipe is at approximately the same temperature. This is a valid assumption for heat pipes as a two-phase system remains at a relatively stable temperature. The bulk temperature of the air was measured using a sheathed ungrounded thermocouple (type J) and placed about 5 cm in front of the pipe at approximately the center of the duct as shown in Figure 3.15.

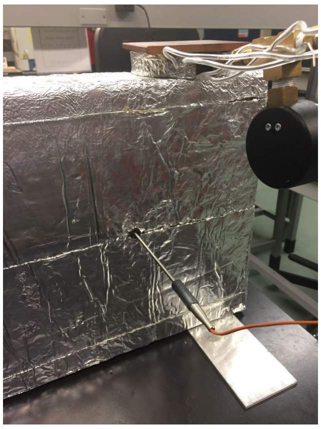

Figure 3.15: Thermocouple location for bulk air temperature measurements

Finally, the bulk velocity of the air for both the low and high setting was estimated based on continuity using the specifications from the manufacturer in cubic feet per minute (CFM) and the proportion between the cross-sectional area of the duct's inlet and the duct itself. However, in order to confirm the values for the estimated bulk velocities as adequate measurement tools were not available, Ansys® Fluent, a computational fluid dynamics (CFD) software was used. CFD is based on the continuum of particles in motion and is used to solve for variables such as pressure and temperature at any point in a domain with numerical methods. In a Eulerian approach, each point is observed within a fixed space. In this control volume, for incompressible flows where density is considered constant, both the conservation of total mass and linear momentum are satisfied. The software describes these conservation equations as partial differential equations (PDEs), and uses a control volume finite difference technique which discretizes the PDEs into algebraic equations. The solution domain has different types of boundary conditions such as a no-slip condition for walls where velocity is considered to be zero. The set of algebraic equations are formed in such a way that the neighboring points are considered to include the effect of these boundary conditions by interpolation. Finally, once initialized, the solver iterates for the coefficients of the algebraic equations in an implicit manner using the default SIMPLE (semi-implicit method for pressure-linked equations [60]) procedure until the residual of each conservation equation is satisfied within a tolerance.

The set of conservation equations will vary depends on the type and behaviour of flow, and whether the problem is a function of time (transient) or steady-state. The Reynolds number is indication whether the layers in the flow are smooth (laminar) or mixing (turbulent). It is common practice that if Re is greater than 2100, the flow is taken as turbulent. In this case, since the maximum Reynolds number was calculated to be over 2100 for both low and high flow rate setting, the fluid flow was deemed to be in the turbulent regime and incompressible with a Mach number well below 0.3. The k-ϵ model was therefore used to solve for the bulk velocity of the air at the set plane before the bottom heat pipe. In this model, the Reynolds-averaged Navier-Stokes (RANS) equations are used with the additional term being the Reynolds-stress. The Boussinesq hypothesis is commonly used to express the Reynolds-stress in terms of known quantities during the iteration process such as the mean velocity gradient, however the turbulent viscosity is still unknown. Thus conservation equations are used in addition to momentum and energy to solve for the turbulence quantities: the turbulent kinetic energy (k) and turbulence dissipation rate (ϵ), which can then be used to calculate the unknown turbulent viscosity. Finally, this can be used in the RANS equations in order to solve the system of equations. There are several forms of the turbulent transport equations in the k-ϵ model, however, the standard one was used which is set as default in Fluent. [61]

The geometry was designed using SolidWorks® and imported to Ansys® workbench. Using Design Modeler in the Ansys® workbench, the edge to surface tool was used to place caps at the inlet and outlet. The fill tool was subsequently used to create the fluid domain in between the two caps. The stability and speed of the solver towards the set residuals were found to be facilitated by converting the domain to polyhedral cells. Polyhedral cells have been found to better handle re-circulation flows compared to hexahedral cells, which is the case due to the effect of the flow modifiers (as shown in Figure 3.3)[62]. The momentum, continuity, k and ϵ equations were set a tolerance of $1e^{-3}$. The energy equation was set to a tolerance of $1e^{-6}$. The boundary conditions included the inlet velocity from the specifications of the heat gun, a pressure-outlet with zero gauge pressure at room temperature, and the pipe and duct walls having a no-slip condition. Since the energy equation is used, thermal boundary conditions were implemented. The duct is subject to heat loss to the environment through convection and radiation and so a mixed boundary condition was used based on the ventilation in the room and the emissivity of the reflective insulation used. The values used for the boundary conditions can be found in the Appendix. The properties of air were averaged between the inlet temperature and the temperature of the pipe which taken from the deemed steady-state temperatures from experiment. Although it was of interest to determine the bulk temperature of the air in the duct, it was rather important as previously mentioned to confirm the bulk velocity of the air in order to better approximate the heat captured by the TEG. A plane was therefore set as a surface monitor at the same distance from the pipe as the measurement for the bulk temperature of air was taken as shown in Figure 3.16. The bulk velocity was computed by selecting to solve for velocity magnitude at the plane using an area-weighted average. A grid independence test was done for a range of grid sizes by increasing the relevance (see Tables 5.11 and 5.12). Finally, the computed bulk velocity was compared to the estimated value from the continuity equation as previously mentioned. As there are two different settings from inlet velocity from the source of heat, only two cases were analyzed to confirm the bulk velocity for both flow rate settings. The first being for the low velocity setting with an inlet temperature of 550F and the second for the high velocity setting with an inlet temperature of 1100F.

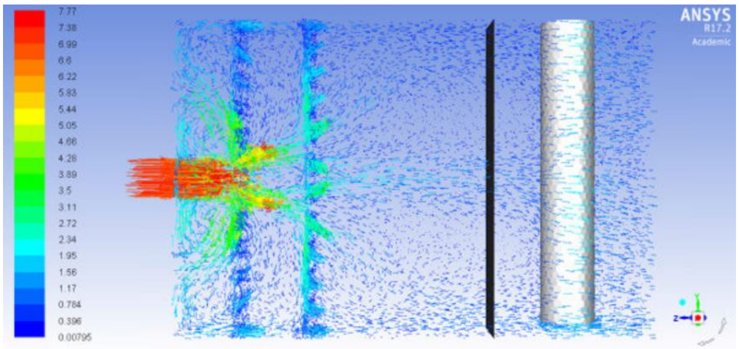

Figure 3.16: The placement of the surface monitor and the vector field for the velocity of the high flow rate setting

The following empirical relation (Eq 3.11) has proven to be valid for a Reynolds number evaluated at the film temperature from 0.4 to 400,000 [63].

$$Nu = \frac{hd}{k_f} = C(\frac{u_\infty d}{\nu_f})^n Pr_f^{1/3} \tag{3.11}$$

where the constants C and n are a function of the Reynolds number (see Table 5.5 in the appendix) and the subscript f represents the properties being evaluated at film temperature which is approximated as the average of the bulk air temperature and the temperature of the wall. For all necessary values for air properties, a table for the properties of air at 1 atm [64] was used and retrieved as a 3rd order polynomial using the polyfit function in Matlab.

The heat flux is a product of the heat transfer coefficient and the difference between the air and wall temperature as shown in Eq. 3.12.

$$Q''(W/m^2) = h\Delta T = C(\frac{u_\infty d}{\nu_f})^n Pr_f^{1/3} \frac{k_f}{d} \Delta T \tag{3.12}$$

Finally, the heat captured by the TEG is thus a product of the heat flux and coverage area of the pipe including the surface area under the pipe (Eq. 3.13).

$$Q_{in}(W) = Q''A \tag{3.13}$$

3.6 Results

3.6.1 Experimental results

The temperature profiles for two test runs are shown in Figures 5.15 and 5.16 in the appendix. The flow rate was fixed at the low setting (8.8 CFM) for a set of tests done for inlet temperatures of 500F(260°C), 600F(316°C) and 700F(371°C). The temperature profiles for the hot-side and cold-side temperatures were fitted using the curve fitting toolbox from Matlab. For each profile, the *diff* function was used to determine the change in temperature over change in time and a limit was set of 0.001°C/s to obtain a temperature range which is deemed as steady-state.

Table 3.17: Mean cold-side temperature and hot-side temperature with standard deviation for the low flow rate runs

Run	T_h(°C)	T_c(°C)	$\Delta T(°C)$
1	48.5 $_{std:0.2}$	27.5 $_{std:0.2}$	21.0
2	52.4 $_{std:0.1}$	28.5 $_{std:0.1}$	23.9
3	55.1 $_{std:0.2}$	29.4 $_{std:0.6}$	25.7

The inlet temperature of the heat gun was then varied from 500F(260°C) to 1100F($\approx$ 593°C), in intervals of 100F($\approx$ 56°C) and the flow rate was changed to the high setting (17.7 CFM). The temperature profiles for the hot-side and cold-side temperatures were also fitted using the curve fitting toolbox from Matlab. For these tests, the limit was also set to 0.001°C/s and the results can be found in Table 3.18.

Table 3.18: Mean cold-side temperature and hot-side temperature with standard deviation for the high flow rate runs

Run	T_h(°C)	T_c(°C)	$\Delta T(°C)$
1	58.4 $_{std:0.1}$	32.6 $_{std:0.1}$	25.8
2	67.0 $_{std:0.2}$	34.5 $_{std:0.2}$	32.4
3	73.4 $_{std:0.2}$	38.5 $_{std:0.2}$	34.8
4	82.2 $_{std:0.4}$	44.3 $_{std:1.0}$	37.9
5	86.9 $_{std:0.2}$	44.2 $_{std:0.3}$	42.7
6	88.9 $_{std:0.1}$	46.2 $_{std:0.4}$	42.7
7	104.9 $_{std:0.1}$	53.1 $_{std:0.4}$	51.9

The results for experimental power output as a function of inlet temperature for the different flow rate settings are plotted in Figure 3.19.

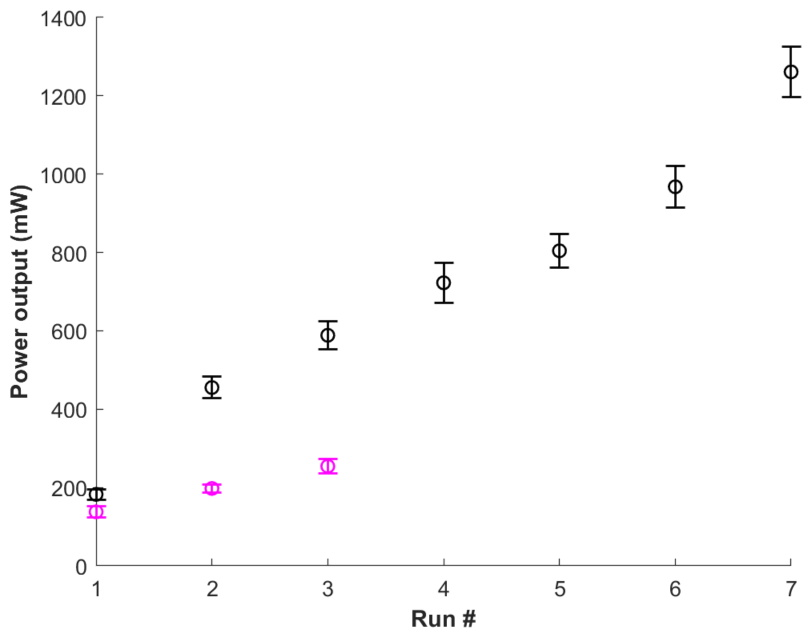

Figure 3.19: Power versus different inlet temperatures (500F to 1100F) in increments of 100F for each run for low (magenta) and high flow rate (black)

3.6.2 Comparison to modeling results

Figure 3.20 below compares the modeling results from the simplified and detailed TEM model and the experimental results for three runs at different inlet temperatures and the low flow rate setting. The values for T_h and T_c as input to the model are found in Table 3.17.

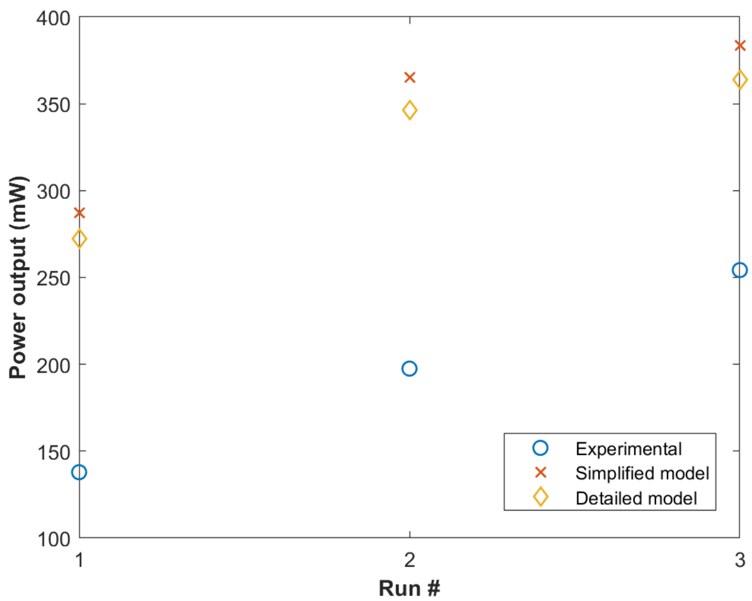

Figure 3.20: Power output comparison versus different inlet temperatures (500F to 700F) in increments of 100F for each run for low flow rate

Figure 3.21 compares the modeling results from the simplified and detailed TEM model and the experimental results for three runs at different inlet temperatures and the high flow rate setting. The values for T_h and T_c input to the model are found in Table 3.18.

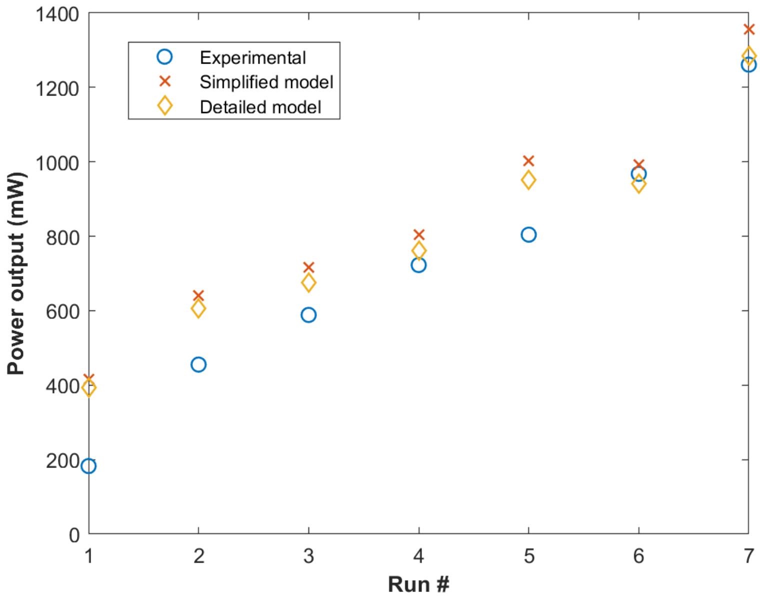

Figure 3.21: Power output comparison versus different inlet temperatures (500F to 1100F) in increments of 100F for each run for high flow rate

3.6.3 TEG efficiency

The mesh size for the computed bulk velocity using Ansys Fluent ranged from 15,909 nodes to 230,997 nodes using five different sizes altogether. The lowest percent difference was found to be between the two finest mesh sizes at less than 2% for both the low and high inlet velocity settings. The results are found Tables 5.11 and 5.12 in the Appendix. The efficiency(using equation 3.14) was then calculated using the average power output for the deemed steady-state temperature range as shown in Figure 3.19 and the heat captured by the TEG for the low and high flow rate runs. The heat captured by the TEG was calculated using the empirical formula as described previously by Equations 3.11.

Table 3.22: Mean bulk temperature of air and mean wall temperature and calculated heat captured for the low flow rate settings

Run	T_{air}(°C)	T_{wall}(°C)	$Q''(W/m^2)$	$Q_{in}(W)$
1	112.4 $_{std:0.2}$	62.8 $_{std:0.1}$	306	15.2
2	128.4 $_{std:0.3}$	68.5 $_{std:0.1}$	369	18.3
3	143.3 $_{std:0.0}$	73.1 $_{std:0.1}$	432	21.5

Table 3.23: Mean bulk temperature of air and mean wall temperature and calculated heat captured for the low flow rate settings

Run	T_{air}(°C)	T_{wall}(°C)	$Q''(W/m^2)$	$Q_{in}(W)$
1	132.1 $_{std:0.3}$	76.9 $_{std:0.2}$	470	23.2
2	150.7 $_{std:0.4}$	87.1 $_{std:0.2}$	540	26.8
3	168.6 $_{std:0.3}$	96.4 $_{std:0.2}$	614	30.5
4	190.8 $_{std:0.4}$	109.8 $_{std:0.2}$	689	34.2
5	205.5 $_{std:0.1}$	117.0 $_{std:0.3}$	752	37.4
6	222.2 $_{std:0.1}$	128.7 $_{std:0.1}$	794	39.4
7	240.7 $_{std:0.7}$	143.0 $_{std:0.4}$	830	41.2

$$\eta = \frac{P_{out}}{Q_{in}} \cdot 100 \tag{3.14}$$

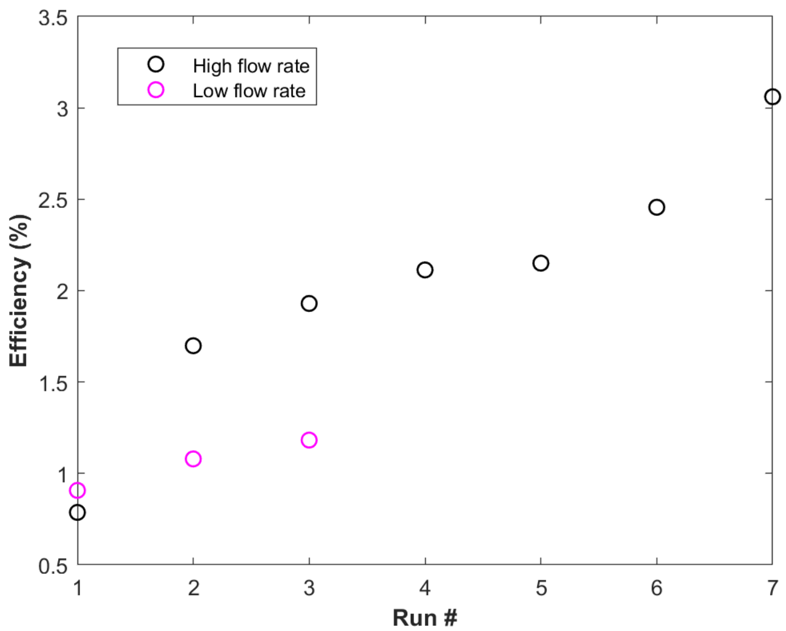

Figure 3.24: Efficiency comparison versus different inlet temperatures (500F to 1100F) in increments of 100F for each run for both low (magenta) and high flow rate (black)

3.7 Discussion

3.7.1 Experimental results versus modeling results

The detailed model is slightly more accurate relative to the simplified model when compared to the experimental results. There are many factors that may be influencing the deviation between model and experiment. An attempt will be made to describe them and to explain how these factors may influence results.

As described in section 1.5, the thermal and electrical contact resistance can affect TEM performance. This was not taken into account with either model, which could otherwise be included in the thermal resistance network of the model if these values were known and accurate. An indication of the influence of thermal contact resistance is the decrease in the difference between the experimental and modeling values as the average system temperature increases for almost all of the test runs. Even though, the thermal contact resistances were not included implicitly, in the thermal resistance network, the total thermal resistance on the hot-side were aggregated as well as those on the cold-side. This may have been overestimated which could very well point that some of the differential value of the unknown overestimation and the actual value can be thought of as allocated to a thermal contact resistance in an explicit manner according to framework of the model. If it was underestimated then the results should have been closer to the model for the initial low system temperature test runs. The surfaces between the thermal spreaders and the TEMs are actually comprised of micro-asperities interacting with each other based on the morphology of each material's surface and external variables affecting it. The thermal contact resistance has been previously found dependant on parameters such as pressure, surface roughness and hardness[41]. According to this mathematical relation, the increase in average system temperature could have decreased the thermal contact resistance by increasing the pressure on the surface of the TEMs through the thermal expansion of the thermal spreaders as well as the TEMs. By decreasing the thermal contact resistance, more heat would be supplied to the TEMs and thus power output can increase. This could be interpreted as the experimental results becoming closer to the modeling results due to increase in system temperature as it reaches the value for total thermal resistance in the model. The model could be adjusted to account for a varying total thermal resistance on the hot- and cold- side of the TEMs as a function of temperature, potentially even varied differently for each side.

The thermal resistances due constriction and spreading (heat transfer from a larger surface area to a small surface area and vice-versa) were also not taken into account, which could be also included in the thermal resistance network and together with the thermal contact resistance can further bridge the gap towards the actual total thermal resistance at the hot- and cold-side of TEMs. These are only some of the factors to consider to obtain a closer margin of error between the model and experimental results.

The setup itself has an effect on the repeat-ability of the experimental results. The bench-top prototype was re-setup after each test period, and although the fasteners that hold the two thermal spreaders together were tightened to a maximum by hand, the pressure and thus contact resistance may indeed vary for each test period which can lead to inconsistent results. The need to include a variability in pressure, when coming up with a value for thermal contact resistance can be avoided by using a mechanical pressure gauge in the experimental set-up and ensure a certain value is consistently reached test for test.

Another influencing factor is the method used to translate the raw data from the manufacturer into a form that can be easily used as an input to the model. The temperature-dependant properties were obtained using a webplot digitizer [65] which provides a table of data points when manually selecting points from the plots of electrical conductivity, Seebeck coefficient and thermal conductivity. The polyfit function from Matlab was then used to fit the data using a polynomial. The values for each properties are thus between the points are interpolated and are extrapolated before the first point which starts at approximately 50°C. The issue is that these values therefore may not be accurate when the model needs to take either a value between two points, before the first or after the last point according to the raw data set.

Furthermore, the model is based on a uni-couple for the n-type and p-type leg. Hence, the results for a one couple were simply multiplied to obtain the power output of 126 couples for each TEM and four TEMs altogether. This may be an inaccurate approach given again, the influence of electrical and thermal contact resistances. It is recommended to further investigate as to how accurate the assumption is that both the electrical and thermal contact resistances scale linearly with the number of couples in the device.

Although there is indeed a difference between model and experiment, the results are not entirely far off from one another (as shown in Figure 3.21). The model can still be a useful tool to obtain a good estimate of potential power output of a device by knowing the geometry of the couple, temperature of the hot and cold-side of the TEMs, the temperature-dependant properties of the thermoelectric materials and the thermal and electrical properties of the substrate and interconnects.

3.7.2 TEG efficiency

The efficiency is quite low as expected for a TEG in this temperature range, however the method used to calculate using the semi-empirical method does not fully capture the effect of the hot-side and cold-side heat exchanger. There can be several reasons to make this claim, one is particular is the heat captured by the pipe compared to the heat transferred to the modules. The reason is that there are heat transfer limitations associated with heat pipes as described in section 3.2. These can be quantified, although several variables would have to be known, in particular the water vapor temperature and saturated water vapor pressure as the system reaches a thermal equilibrium or the deemed steady-state in this case. Given the relationship between temperature and pressure in the Clausius-Clapeyron equation, with one of these variables known, the other can be as well given a set of reference temperature and pressure. The wall temperature which was measured through the experiments, can be used as an initial approximation to determine the heat transfer limits and compare them to the heat captured by the bottom heat pipe. If the heat captured is within the limits, then it can be valid to claim that the heat captured is essentially the heat transferred to the thermoelectric modules. However if not, the heat transferred to the TEMs is therefore hindered and a return to the design phase for heat pipes is necessary in order to maximize performance. Also to note, the limitations would not be the only factor hindering this. There are also heat leakages at the walls of the condenser, despite insulation being used in this area some of the heat may have been lost via condensation on the walls rather than the thermal spreader.

Another factor affecting the calculated efficiency values is the location of the bulk air temperature measurement which was input to the semi-empirical relation. If the thermocouple was placed closer to the heat source, the calculated heat into the TEG would be different than if it was closer to the heat pipe, as what was deemed the bulk temperature would vary. The choice of placement was due to the size constraint between the flow modifier and the pipe, and the thermocouple was arbitrarily placed about three quarters from the flow modifier to the pipe. To avoid this uncertainty, the effect of the thermocouple placement at different positions along the length of the duct as well as the cross-section could be closely examined. The same could apply for the bulk velocity of air. However, in terms of measurements along the length, according to the simulations (see Figure 3.16), the vector field does not show significant variations around 4-5cm in either direction from this location, however this is not the case for the variations in the cross-section as seen in Figure 5.13 in the Appendix.

3.7.3 Thermal losses

The values of temperature obtained in the fluid domain from simulations are assumed to be inaccurate. The reason being that the temperature measurements of the bulk air are significantly lower that the values obtained from simulation. The major factor involved in such a difference must be from the thermal losses in the system which were not adequately or precisely taken into account.

First, although insulation was used to cover the duct, there are still exposed inner faces, which can be subject to heat loss due to radiation if at different temperatures which is likely to be the case. Also, the insulation is also not fully effective, however this was partly considered based on setting a boundary condition using the ambient temperature and the emissivity of the reflective insulation used on the outside of the duct. The convection on the outside walls of the duct and conduction through the duct walls also lead to heat loss or perhaps even additional heat via conduction by-passed through the support ring between the duct walls and the bottom thermal spreader. To account for convection of the outside walls at least, an arbitrary heat transfer coefficient of 10 $\frac{W}{m^2K}$ was used in an attempt to account for the heat loss presuming natural convection was occurring, as well as the ambient temperature, which is again, was also an assumption. Although the bottom of the duct was placed on a steel bench, a boundary condition for natural convection was set at 5 $\frac{W}{m^2K}$, even though the mode of heat transfer is via conduction, in an attempt to account for heat loss at that surface. As seen in the appendix, the bulk temperature of air and the contours on the plane in front of the bottom heat pipe are quite far from the temperature measurements. For example for run 7, the bulk temperature was measured at 241°C, where as the simulations result in a bulk temperature of 417°C at the plane. Overall, the simulated heat loss was far from accurate, and deemed underestimated, as too many unknown parameters were assumed as described. Alternatively, another fluid domain may used to simulate the room, however the level of complexity and the computational power needed to solve the much larger domain and coupled interfaces would be greatly increased.

3.7.4 Future considerations

The goal of using computational fluids dynamics was rather to solve for the bulk velocity of air, instead of having to obtain physical measurements, in order to estimate the heat captured by the pipe using the empirical relation for a cylinder in a cross-flow. Regardless of the attempt to take into account the heat loss in the system, from a decoupled point of view, this goal was achieved. However, the inlet velocity of the air was assumed to be exactly the given specifications from the manufacturer of the heat gun which should be verified. Various types of flow-meters can be added to the experimental apparatus used at both the inlet and moved throughout the duct's cross-section to obtain a more accurate value for the bulk velocity of air. This would result in a more independent comparison between the estimated value and the numerical results for the bulk velocity of air.

In terms of the numerical method used, for the k-ϵ model, the wall adjacent cell heights are important to investigate [61], as it effects the solver's selection for which model is used to solve turbulence quantities. Although the default mesh used provided adequate results compared to the estimate, in future work, attention should be given to this when building a customized mesh as calculations can be done to estimate the cell height based on the Reynolds number, which can be a good starting approximation [61].

According to the velocity magnitude contours (see Figure 5.14 in the Appendix), there is still a greater bulk velocity at the center of the duct and also significantly greater around the top and bottom areas compared to the rest of the cross section. This is indication that the flow modifier design can be indeed improved. In this regard, it is also recommended that the duct is lengthened after the heat pipe to ensure the flow is fully developed so that the heat transferred to the pipe and thus flow of hot air is not significantly affected by the outlet due to proximity.

The empirical relation for a cylinder in a cross-flow does not capture the full extent of the heat pipe as a two-phase system and its ability to act as a superconductor. It is therefore proposed to use computational heat transfer and fluid dynamics to solve for the heat captured by the pipe by taking heat loss into account and without using the pipe wall temperature obtained from experiment. In addition, the cold-side heat exchanger should be added to fully couple the effect of the TEG on the temperature and velocity in the fluid domain. There is indeed an added complexity with using a multi-phase model for inside the heat pipe, however a simplification can be made by assigning an effective thermal conductivity to a solid pipe in a cross-flow using a thermal resistance network [66].

Overall, the efficiency of the TEG could be increased if the heat pipe parameters were optimized according the amount of heat captured initially, that is if the threshold of the lowest quantified limit surpasses the heat captured, and is consequently increased so that the heat transferred to the TEMs is maximized. To achieve a valid result, is it necessary that the heat captured by the pipe be accurately simulated as well the variables associated to the heat transfer limitations accurately estimated.

To increase the performance of the TEG, other than supplying more heat to the TEMs, the TEM materials and geometry as well as the occupancy ratio can be optimized for a certain temperature-range as described in section 1.4. The occupancy ratio is the covered area of TEMS over the thermal spreader area. A lower occupancy ratio can increase the heat supplied to the TEMs but comprises the power output [67]. Also, a maximum power point tracker (MPPT) algorithm in a power conditioning circuit can be used increase the power output by varying the load resistance to fulfill the maximum power transfer theorem according to the TEMs electrical configuration and variables such as temperature fluctuations [68].

There are indeed a major design issue that should be addressed in terms of using this concept as a practical solution. It would be necessary that the cold-side heat exchanger be re-conceptualized as it was not completely passive. An ideal approach would to use forced convection with air or better yet, a heat transfer fluid, however that would require a parasitic load through the need to pump or circulate a fluid. Another option would be to increase the height of the top heat pipe in order to increase the condenser area and reject as much heat as possible. The increase in axial length however will need to be analyzed to determine its effect on the heat transfer limitations while considering the heat being supplied by the cold-side of the TEMs. It therefore recommended to further this work through the design of a fully or almost fully passive heat dissipation unit using natural or mixed convection. This may be difficult to achieve, however, it is crucial step towards a self-reliable, sustainable solution.

Although not reported or investigated in this work, error analysis is an important topic to include in this type of work. With physical measurements, the errors lead to uncertainty in results and thus should be properly reported [69]. In this case, the experimental power output using a circuit that include the shunt resistor, the mini computer, there is a propagation of uncertainties than can be estimated. As well as the modeling results which include temperature measurements from thermocouples and a data acquisition device. The calculation of efficiency can also to be considered, which also uses thermocouples, data acquisition, flow rate from the heat gun specifications and the empirical formula used to obtain the heat captured by the TEG.

Chapter 4

Recommendations for application

In order to implement this solution for industrial processes, The TEG should fulfill the following criteria:

- must be designed for safety on the existing structure in the case of a retrofit
- is cost-effective over its' lifetime
- is a sustainable technology compared to alternative solutions

To address these points; computational software tools that include mechanical stress analysis, optimization algorithms and life-cycle analysis are recommended to be used in the planning phase. For example, in the case of a retrofit, all necessary constraints such as the maximum load allowed on the existing structure and the space available for the TEG can be input to a software to output key parameters of possible solutions such as geometry and number of heat exchanger sections in a modular design. The structural and thermal analysis as well as material selection for safety purposes should be done to provide adequate design solutions in a case-specific manner. This can be completed with commercially available software that use the finite-element method such as Matlab or Ansys. Some general guidelines however for cost-performance and life-cycle analysis will be provided.

4.1 Cost-performance analysis

The performance of thermoelectric devices depends primarily on geometry and the temperature-dependant properties of materials used. Thus, for the modular solution to be optimized for maximum performance, the array of heat pipes to capture and concentrate the heat can be split into sections for industrial applications [25]. In this sectioned design (as shown in Figure 4.1, when extracting heat in the flow of exhaust gases, the temperature would decrease along the length as the available heat is extracted. Therefore, each section can then be optimized for its' respective temperature range and use thermoelectric materials accordingly. The objective is to be cost-effective, so in this method, the number of sections and preliminary design of each can be determined to both maximize the total power produces and minimize the overall cost. This will discard sections that are worth adding based on the minimal power they produce, and the cost associated to them.

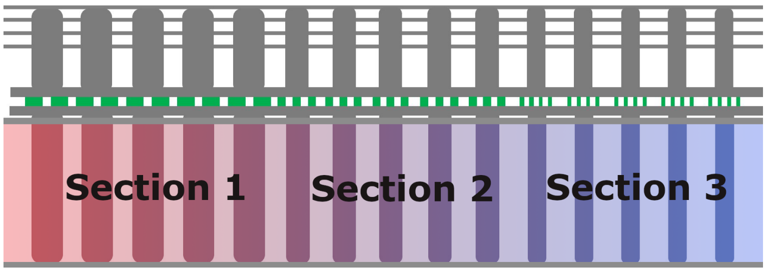

Figure 4.1: Schematic of a sectioned design for a TEG with a gradient of color that represents a decrease in average system temperature

This can be done using Matlab or Simulink with the optimization toolbox. In this case, the problem can be described using heat transfer correlations to determine the cumulative heat captured by the sections coupled with a TEM model as described in the previous section to calculate the cumulative efficiency. The main components can also be prescribed a cost function in terms of geometry, density and cost per weight. Matlab's function *fmincon* can then be used by formulating objective functions with the mathematical description to minimize power output over cost in terms of the desired variables to solve for, such as number of sections, pipe spacing and both TEM occupancy ratio and geometry. The user finally provides initial guesses for the variables along with a set of equations to describe the constraints such as the space available, and geometric size range of components, allowable hoop stress for the pipes, the allowable pressure drop in the duct, a threshold for the power output over cost etc.

4.2 Life-cycle analysis

A life-cycle analysis (LCA) comprises of scientific and technical analysis of potential impacts associated with a product or system. It is usually combined with a life-cycle assessment, which is used for decision-makers to evaluate political decisions based on the analysis. Specifically, LCA is unique as it includes in-direct impacts such as those embodied in materials and equipment, and materials/facilities used to manufacture tools and equipment for the processes in question. In general, the impacts are expressed relative to a functional unit and integrated over space and time. [70]

It is rather difficult to acquire all the necessary data required for a considerable time to do a credible LCA. However, there has been developments in the field as a result of standards from independent, international bodies such as ISO to create systematic frameworks.

LCA is not a tool used to determine the ultimate solution, but when done with careful interpretation, no bias and an uncertainty analysis, is it useful in providing more information to decision-makers and/or stakeholders for products or systems. It is used rather as a comparative tool, for example when analyzing energy systems, it can be used to compare technologies that are components of the system, the system itself altogether or even different scenarios in the energy sector as a whole.

The purpose of the analysis must be first formulated through the development of both a goal such as the intended application and a scope such as describing the function, initial choices on system boundaries and the quality of data.

Energy systems can be described by a single chain of energy conversions can be analyzed based on site- and technology specific components which includes side-chains as described earlier by indirect impacts [70]. For a TEG retrofit to recycle waste heat, a partial system analysis can be done, which would compare different state-of-the art products that provide the same function. This can be done by using a unit energy of say 1 kWh as a functional unit, and focus on part of the system or chain such as only the conversion, transmission part taking into account indirect impacts.

This can become complicated as there are many types of impacts besides environmental impacts that can be included in an LCA and many impacts are difficult/complex to quantify through models. There are economic impacts, such as evaluating net-present values of expenses, and imports/exports and employment on the national economy. Environmental impacts are also detailed which include and not limited to: land use, noise, visual, local pollution of soil, water, air and biota, regional and global pollution's and other impacts on the Earth at a larger scale such as the atmospheric system. There are also social impacts, impacts on security and resilience, impacts on developmental and political impacts that can be considered. [70]

What to include depends on the context of the study which could be a function of the development of a energy technology or energy system. For example, a more general LCA can be used for choosing a technology in the planning phase by comparing different products in different scenarios. In the case of a TEG, the LCA can be used to compare to technologies with the same purpose such as heat recovery steam generators (HRSG) and organic Rankine cycle (ORC) for different scenarios such as space available for a retrofit or the quality (temperature of waste heat) taking into account social, economic and environmental impacts.

After finding the better scenarios or technologies best suited for a scenario, this can be followed by a more specific LCA for the implementation phase, for scaling and/or choosing a location. For example, in energy systems with emissions, dispersion models are typically used to estimate the fate of emissions in terms of the concentration of each species in space. This could take into account population density around the origin of these emissions and how they would change each species total concentrations compared to a predefined threshold. This specificity can lead to complicated analysis and perhaps inaccuracy as uncertainty can accumulate through allocation and accounting when quantifying impacts. It is therefore suggested to use scenarios, to make valid assumptions on what to include as impacts according to the purpose of the study and present and analyze/interpret the results in an unbiased manner, potentially according to impacts that are heavily weighted by the stakeholders involved and/or decision makers.

Chapter 5

Outlook

The proposed direction of this work is based on a bottom-up approach to further develop this concept from thermoelectric materials to thermoelectric generators at a systems level.

The use of artificial intelligence (AI) can be a useful tool for the discovery of new candidates. A recent study demonstrates the ability to predict materials with potentially good thermoelectric properties. They did so by using abstracts as the data set, and an algorithm based on combinations of words in a mathematical manner to find potential candidates without the author implying anything about thermoelectricity or its applications. When observing a large set of abstracts only before 2008, the algorithm was able to predict potential candidates, which happened to be in good correlation with the thermoelectric materials actually being studied in the period after this [71].

With a range of possibilities, what to test can be assess by advanced computational techniques that can accurately predict the performance of materials without any prior testing. This can be a low-cost step, depending the availability of the simulation tools, to verify and confirm their potential. A life-cycle analysis of these candidates is recommended to be done at the early stages as opposed to the application stage. The best performing thermoelectric materials in the low temperature range are known to be compounds mainly composed of bismuth (Bi) and tellurium (Te). These are scarce elements as seen in Figure 5.1, inherently costly and also have been found to have high relative emissions in the mineral processing stages [72]. The research and development of materials using abundant elements/compounds is a key aspect in forming a sustainable TEG for industrial applications with potentially low environmental impact and positive economic impact.

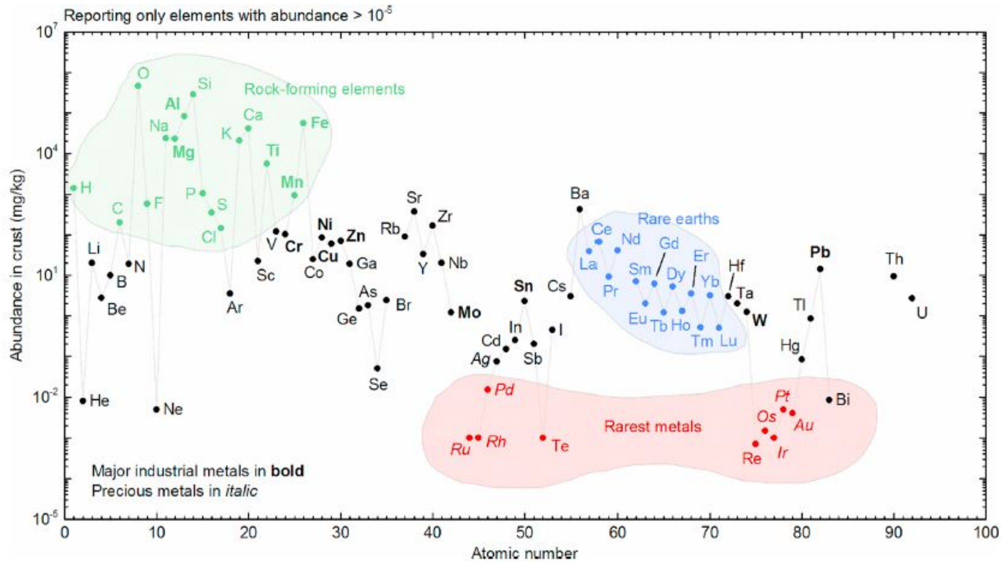

Figure 5.1: Estimated abundance of elements in the earth's crust [1]

Some candidates currently being studied are oxide-based thermoelectrics such as zinc oxide (ZnO) as an n-type and nickel oxide (NiO) as a p-type, which can have good thermoelectric properties when doped with aluminium (Al) and lithium (Li) respectively, for high temperature applications. In order to investigate their potential, samples were synthesized and properties measured as a function of temperature. Using the detailed semi-empirical model without any thermal resistances, the power per area was determined for a ZnO-NiO based couple by implementing Matlab's polyfit function on the property data obtained. The samples were synthesized using a sol-gel method, however different processing methods could lead to variations in properties, as influencing the microstructure. The Probostat was used to measure the Seebeck coefficient and electrical conductivity. The Seebeck coefficient was measured by suspending the sample between two thermocouple tips to measure temperature at both ends and the voltage between the positive and negative lead of the thermocouples. The electrical conductivity was measured using the Van der Pauw 4-point conductivity method using platinum (Pt) electrodes at four opposite faces positions on one face of the sample. The placement of the thermocouples and electrodes on the sample can influence the results so repeatable testing with these methods are recommended. The thermal conductivity was measured using NETZCH's laser flash technique which follows ASTM standards.

The temperature-dependent properties were then treated similarly to those used in

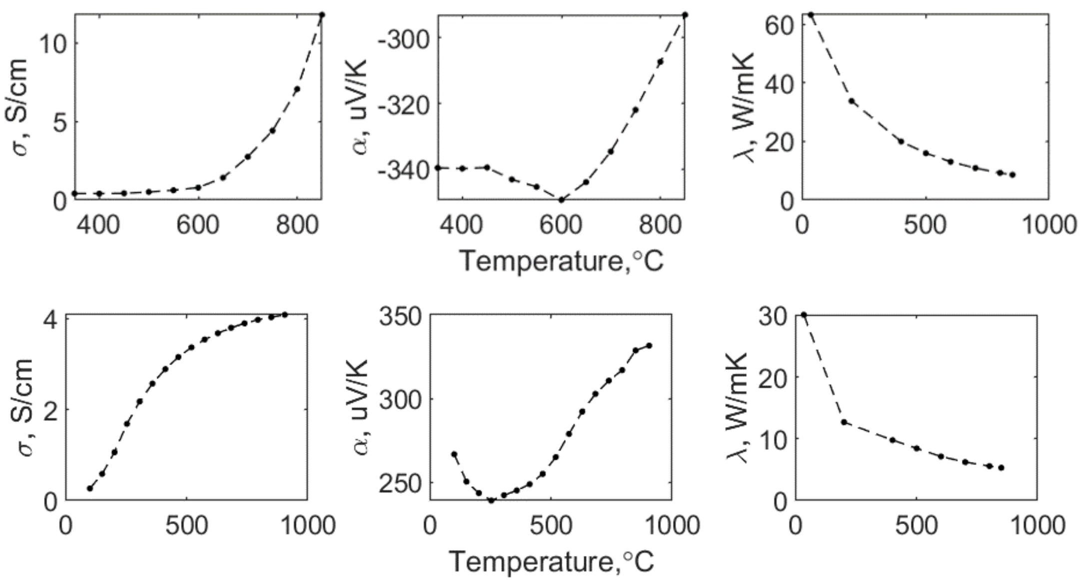

Figure 5.2: Electrical conductivity, Seebeck coefficient and thermal conductivity (left to right, respectively) for samples of $Ni_{0.98}Li_{0.02}O$ (top) and $Zn_{0.98}Al_{0.02}O$ (bottom)

the detailed TEM model in section 3.5.2. Based on a fixed cross-sectional area of $25mm^2$ for each leg, the height of the leg was varied and the power output calculated using the detail model. The hot-side temperature and cold-side temperature was (Th=950°C and Tc=500°C) in order to compare to the performance of a state-of-the-art device found in the literature.

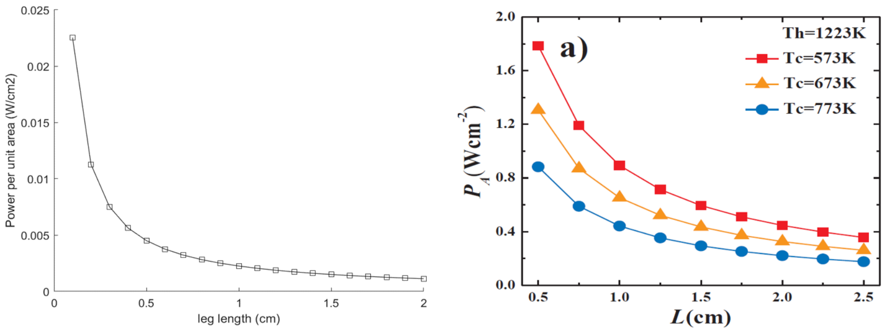

Figure 5.3: Left: Power output per unit area for a NiO-ZnO-based couple . Right: Power output per unit area for a SiGe-based couple modeled based on the devices used in NASA's TEG on Cassini [15]

Although the power output per unit area is found to be around two orders of magnitude greater than the NiO-ZnO couple, the cost per kg however is also around two orders of magnitude greater for bulk SiGe-based materials compared to $Zn_{0.98}Al_{0.02}O$

[73]. With the goal of improving the figure-of-merit as mentioned in section 1.3, in-depth research is required, which can strategically use the process-microstructure-property relationship in engineering materials that pass the materials design stage. This can be coupled with synthesizing samples and testing temperature-dependant properties as done in Figure 5.2 in order to model the performance of a device using bulk materials in a simplified manner.

The next stage in research and development would be on the device level, for thermoelectric modules (TEMs) in this case. This can involve using accurate models with optimization and compatibility factors, to design practical and efficient TEMs and test them over time using reliable apparatuses to study important degradation mechanisms that affect long-term performance and efficiency. This stage could then be fed back to the materials development stage in order to engineer solutions which can overcome the issues found and work towards the overall goal of producing low-cost, long-lasting and efficient devices that are well-suited for a range of conditions.

The coupling of TEMs with heat exchangers in a modular approach is a crucial aspect as to maintain the temperature gradient in a cost-effective manner. Although this thesis demonstrates a concept that can be viable as modular approach for industrial waste heat recovery, there is a need for further work on the systems level. A step towards a realistic solution on the industrial scale can involve the development of a pilot derived from this works' concept. However, the factors limiting the performance of this prototype must first be addressed. The goal of a pilot would be then to validate modeling techniques with experiment to form a testing rig that could be used to predict the benefits of different waste heat scenarios in terms of cost-performance. The developed pilot and software can include other important aspects that were touched upon in section 1.5 to develop a cost-effective TEG. This entire systems approach can then be added as a viable option to a decision-support tool which altogether can further bridge the gap towards the industrial application of TEGs as a state-of-the-art waste heat recovery technology.

There may indeed be different perspectives as to what is the best path to take to realize this concept. Although a bottom-up approach has been described, however it may be, the goal should remain the same: to provide a sustainable technology that is truly beneficial to our society within the ecosystem.

Appendix

The materials for both duct and pipe fabrication were acquired from supplier "Metaux Solution". The mesh and spring were purchased online from "Mcmaster-Carr".

The dimensions of the main components are as following:

- duct: 18.25"x 12.25"x 2.625"
- duct wall thickness: 1/8"
- duct height: 12.25"
- flow modifier distance inlet: 3" and 6"
- bottom pipe diameter and thickness: 2.125" and 0.058"
- bottom pipe height: 12"
- top pipe diameter and thickness: 3.125" and 0.058"
- top pipe height: 4"
- compression spring outer diameter and length: 1.938" and 2"[74]
- retainer ring outer diameter: 3"[75]
- mesh size: 150x150[76]
- thermal spreaders: 4"x 4"x 1/4"
- reservoir: 5"x 5"x 4"
- reservoir bottom plate thickness: 1/8"

Table 5.4: Devices and equipment used for the experimental set-up

Item	Model	Reference
Computer fan	Corsair Air Series™ AF140	[77]
Current sensor	Adafruit INA219 Current Sensor Breakout	[78]
Thermally conductive epoxy	OMEGABOND™ 200 Two Part Epoxy	[79]
Hand pump	Mityvac MV8010	[80]
TEMs	TEG2-126LDT	[56]

Table 5.5: Constants for equation 3.11

Re_D	C	n
0.4-4	0.989	0.33
4-40	0.911	0.385
40-4000	0.683	0.466
4000-40,000	0.193	0.618
40,000-400,000	0.027	0.805

```
%% Thermal Resistances
%Dimensions for one couple

x=0.00222222; %[m] substrate
y=0.005714; %[m] substrate
n_x=0.0037; %[m] interconnect
n_y=0.00135; %[m] interconnect
n_t=0.00001; %[m] interconnect
t_g=0.00012; %[m] graphite thickness
t_cer=0.00069; %[m] ceramic thickness
t_ni=0.01/1000; %[m] nickel thickness
t_cu=0.1/1000;  %[m] copper thickness

%Thermal resistance of graphite layer on substrate
t_cond_g=10; %[Wm-1K-1]
R_g=t_g/(t_cond_g*x*y); %[K/W]

%Thermal resistance of ceramic substrate
t_cond_cer=18; %[Wm-1K-1]
R_cer=t_cer/(t_cond_cer*x*y); %[K/W]
R_subs=R_g+R_cer; %[K/W] %both graphite and ceramic

%Thermal resistance of nickel braze on interconnect
t_cond_ni=91; %[Wm-1K-1]
R_ni=t_ni/(t_cond_ni*n_x*n_y); %[K/W]
```

Figure 5.6: Example code for thermal resistance calculations

Table 5.7: Boundary conditions for the low velocity case used in Fluent

BC	location	value
velocity	inlet	3.1 m/s
temperature	inlet	561K
heat transfer coefficient	bottom	5 W/m2-K
heat transfer coefficient	outer surfaces	10 W/m2-K
emissivity	outer surfaces	0.04
temperature	ambient	298K
temperature	wall	336K

Table 5.8: Boundary conditions for the high velocity case used in Fluent

BC	location	value
velocity	inlet	6.24 m/s
temperature	inlet	866K
heat transfer coefficient	bottom	5 W/m(^{2})K
heat transfer coefficient	outer surfaces	10 W/m(^{2})K
emissivity	outer surfaces	0.04[81]
temperature	ambient	298K
temperature	wall	416K

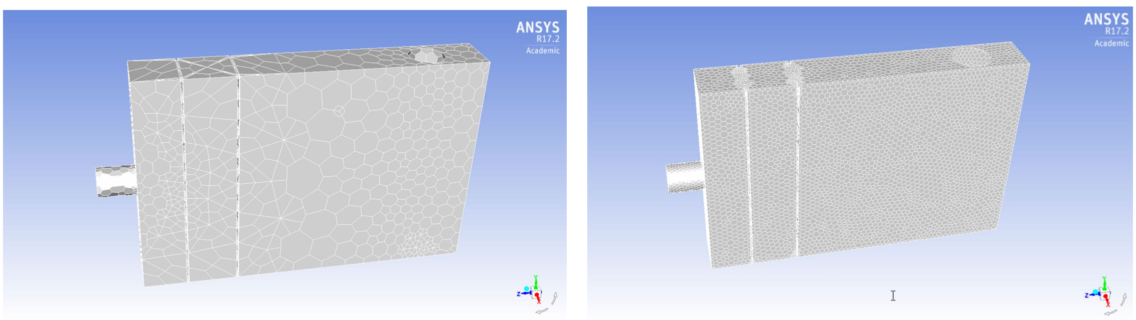

Figure 5.9: Left: Coarse mesh used in first case. Right: Finest mesh used in first case

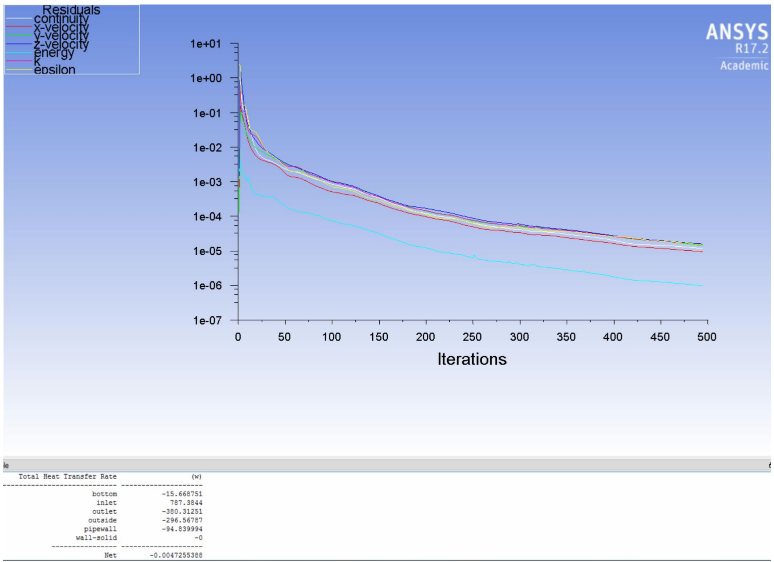

Figure 5.10: Residuals of transport equations (top) and total heat transfer rate (bottom) for the first case at low velocity setting

Table 5.11: Computed average bulk velocity of air for run 1 of the low velocity setting and heat captured by the pipe

Cells	Nodes	$u_\infty(low)$	T_∞	Q_{in}
6503 (rel-100)	15,909	0.172	$189(°C)$	61.2W
13440 (rel-50)	43,057	0.184	$187(°C)$	71.9W
31332 (rel0)	130,618	0.193	$181(°C)$	83.5W
49047 (rel50)	210,771	0.197	$178(°C)$	94.8W
52124 (rel60)	230,997	0.201	$176(°C)$	95.8W

Table 5.12: Computed average bulk velocity of air for run 7 of the high velocity setting and heat captured by the pipe

Cells	Nodes	$u_\infty(high)$	T_∞	Q_{in}
6503 (rel-100)	15,909	0.347	$445(°C)$	201W
20708 (rel-25)	78,870	0.382	$431(°C)$	258W
38938 (rel25)	162,743	0.392	$427(°C)$	294W
49047 (rel50)	210,771	0.399	$420(°C)$	309W
52124 (rel60)	230,997	0.406	$417(°C)$	313W

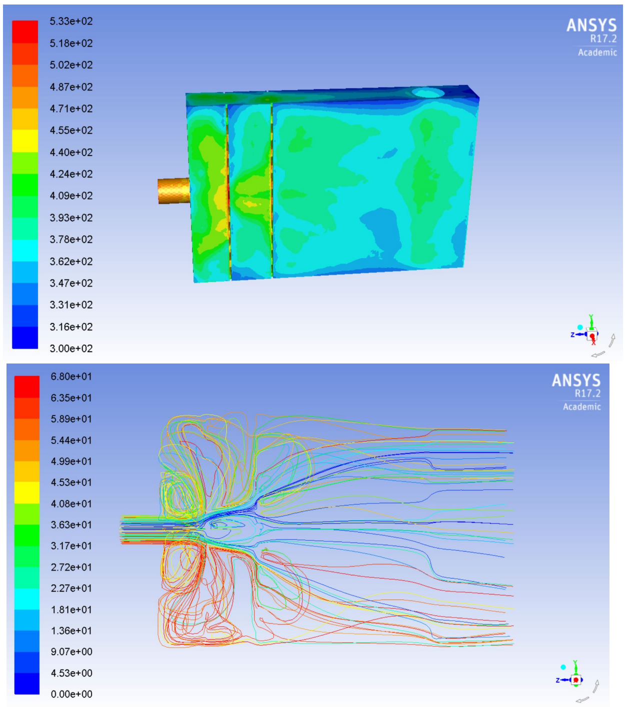

Figure 5.13: Top: Temperature contours for low velocity case. Bottom: Streamlines for particles starting at inlet for the low velocity case

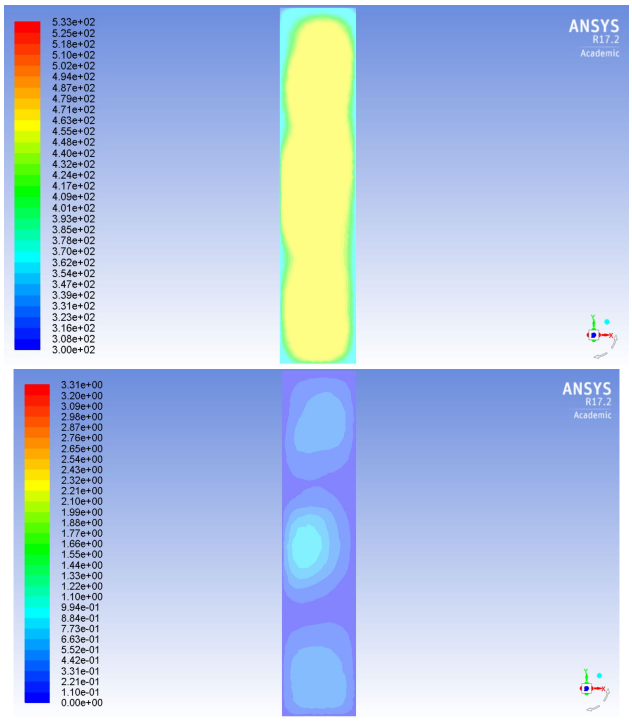

Figure 5.14: Top: Temperature contours at plane before the bottom heat pipe Bottom: velocity magnitude contours at plane before the bottom heat pipe

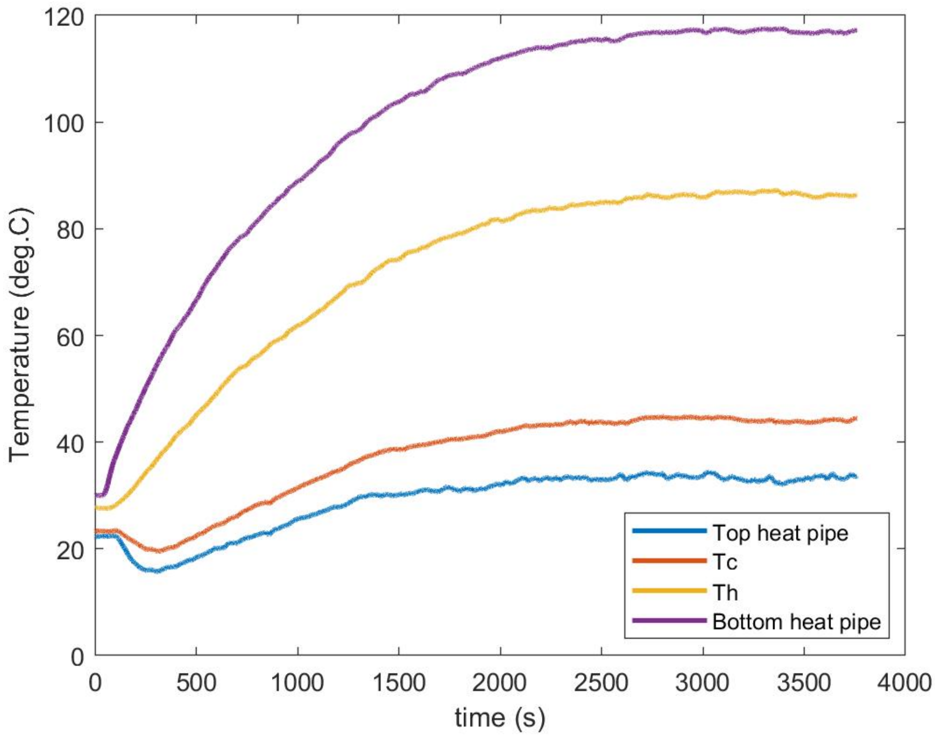

Figure 5.15: Temperature profile for run 5

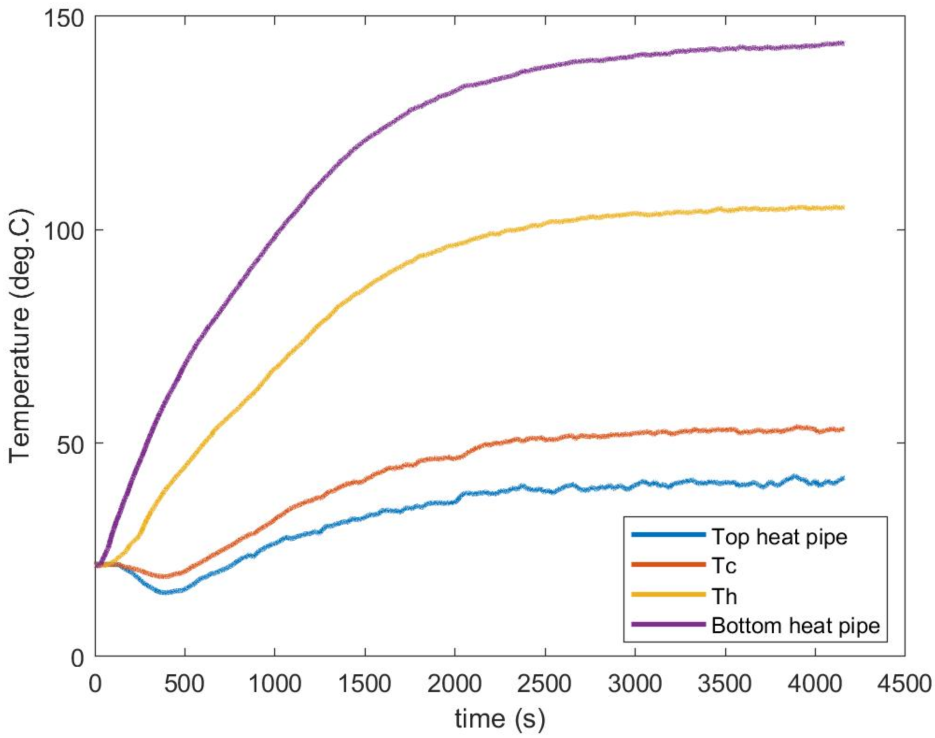

Figure 5.16: Temperature profile for run 7

Bibliography

[1] Davide Beretta, Neophytos Neophytou, James M. Hodges, Mercouri G. Kanatzidis, Dario Narducci, Marisol Martin-Gonzalez, Matt Beekman, Benjamin Balke, Giacomo Cerretti, Wolfgang Tremel, Alexandra Zevalkink, Anna I. Hofmann, Christian Müller, Bernhard Dörling, Mariano Campoy-Quiles, and Mario Caironi. Thermoelectrics: From history, a window to the future. *Materials Science and Engineering R: Reports*, (July), 2018. ISSN 0927796X. doi: 10.1016/j.mser.2018.09.001.

[2] H J Goldsmid and Institute of Physics (Great Britain) Publishers, Morgan & Claypool. The physics of thermoelectric energy conversion, 2017.

[3] BATE. Thermoelectrics, 2013. URL `https://www.mn.uio.no/fysikk/english/research/projects/bate/thermoelectricity/index.html`.

[4] B Lenoir, Jean Lamour Institut, and Ecole Mines. Introduction to thermoelectricity : from basic principles up to devices. 2018.

[5] Materials for Advanced Thermoelectrics, 2015. URL `https://www.sigmaaldrich.com/technical-documents/articles/materials-science/metal-and-ceramic-science/thermoelectrics.html`.

[6] Heonjoong Lee, Jeff Sharp, David Stokes, Matthew Pearson, and Shashank Priya. Modeling and analysis of the effect of thermal losses on thermoelectric generator performance using effective properties. *Applied Energy*, 211(July 2017):987–996, 2018. ISSN 03062619. doi: 10.1016/j.apenergy.2017.11.096.

[7] June F Zakrajsek, Dave F Woerner, and Jean-Pierre Fleurial. NASA Special Session: Next-Generation Radioisotope Thermoelectric Generator (RTG) Discussion.

2017. URL https://solarsystem.nasa.gov/docs/ICT_NextGen_Presentation_August_2017_final.pdf.

[8] Energy Fact Book. URL https://www.nrcan.gc.ca/science-and-data/data-and-analysis/energy-data-and-analysis/energy-facts/20061.

[9] Muhammad Fairuz Remeli, Abhijit Date, Bradley Orr, Lai Chet Ding, Baljit Singh, Nor Dalila Nor Affandi, and Aliakbar Akbarzadeh. Experimental investigation of combined heat recovery and power generation using a heat pipe assisted thermoelectric generator system. *Energy Conversion and Management*, 111:147–157, 2016. ISSN 01968904. doi: 10.1016/j.enconman.2015.12.032. URL http://dx.doi.org/10.1016/j.enconman.2015.12.032.

[10] M Menendez, L Grant, S Yung, and P. Kalous. DAN10: Final Report. Technical report, McGill University, Montreal, 2017.

[11] S W Chi. *Heat pipe theory and practice: a sourcebook*. McGraw-Hill-Hemisphere Series in Fluids and Thermal Engineering. Hemisphere Pub. Corp., 1976. ISBN 9780070107182. URL https://books.google.ca/books?id=4NRSAAAAMAAJ.

[12] Bahman Zohuri. Heat pipe design and technology : modern applications for practical thermal management, 2016.

[13] How Ming Lee and Heng-Yi Li. A mathematical model for estimation of the maximum heat transfer capacity of tubular heat pipes. *Energy Procedia*, 142:3908–3913, 2017. ISSN 1876-6102. doi: https://doi.org/10.1016/j.egypro.2017.12.295. URL http://www.sciencedirect.com/science/article/pii/S1876610217360307.

[14] Chunhui Zhang. *Controlled cooling of permanent mold castings of aluminum alloys*. PhD thesis, McGill University, 2003.

[15] Eurydice Kanimba, Matthew Pearson, Jeff Sharp, David Stokes, Shashank Priya, and Zhiting Tian. A comprehensive model of a lead telluride thermoelectric generator. *Energy*, 142:813–821, 2018. ISSN 0360-5442. doi: https://doi.org/10.1016/j.energy.2017.10.067. URL http://www.sciencedirect.com/science/article/pii/S0360544217317723.

[16] Anatychuk L.I. On the discovery of thermoelectricity by Volta. *J. Thermoelectric.*, 2:5–10, 2004.

[17] The Editors of Encyclopaedia Britannica. Encyclopædia Britannica: Alessandro Volta. URL `https://www.britannica.com/biography/Alessandro-Volta`.

[18] Kashy Edwin McGrayne, S.B, Frank Neville H. Robinson, and Aakanksha Gaur Erik Gregersen William L. Hosch Gloria Lotha Richard Pallardy Veenu Setia Surabhi Sinha Augustyn, Adam. Electromagnetism, 2018. URL `https://www.britannica.com/science/electromagnetism`.

[19] Pastorino G G G. Alessandro Volta and his role in thermoelectricity. *J. Thermoelectric.*, 1:7–10, 2009.

[20] Peter Mark Roget and Society for the Diffusion of Useful Knowledge (Great Britain). *Treatises on electricity, galvanism, magnetism, and electro-magnetism.* 1832.

[21] Lord Rayleigh. XLIII. On the thermodynamic efficiency of the thermopile. *The London, Edinburgh, and Dublin Philosophical Magazine and Journal of Science*, 20 (125):361–363, 10 1885. ISSN 1941-5982. doi: 10.1080/14786448508627771. URL `https://doi.org/10.1080/14786448508627771`.

[22] Rankin Kennedy. *Modern engines and power generators; a practical work on prime movers and the transmission of power, steam, electric, water and hot air.* Caxton Pub. Co., London SE - volumes frontispieces, illustrations, plates, tables, diagrams 27 cm, 1904.

[23] David Michael. Rowe. *CRC handbook of thermoelectrics.* CRC Press, Boca Raton, FL SE - 701 pages : illustrations ; 27 cm, 1995. ISBN 0849301467 9780849301469.

[24] George R Schmidt, Thomas J Sutliff, Leonard A Dudzinski, and Nasa Headquarters. RADIOISOTOPE POWER: A KEY TECHNOLOGY FOR DEEP SPACE EXPLORATION. 2009. URL `https://ntrs.nasa.gov/archive/nasa/casi.ntrs.nasa.gov/20120016365.pdf`.

[25] David Michael. Rowe. *Thermoelectrics and its energy harvesting. Modules, systems, and applications in thermoelectrics.* CRC Press, Boca Raton, FL, nv - 1 o edition, 2012. ISBN 9781466560307 1466560304 9781439840429 1439840423.

[26] Chhatrasal Gayner and Kamal K. Kar. Recent advances in thermoelectric materials. *Progress in Materials Science*, 83:330–382, 10 2016. ISSN 0079-6425. doi: 10.1016/J.PMATSCI.2016.07.002. URL `https://www.sciencedirect.com/science/article/pii/S0079642516300317?via%3Dihub`.

[27] Gael Sebald, Daniel Guyomar, and Amen Agbossou. On thermoelectric and pyroelectric energy harvesting. *Smart Materials and Structures*, 18(12):125006, 2009. ISSN 0964-1726. doi: 10.1088/0964-1726/18/12/125006. URL `http://dx.doi.org/10.1088/0964-1726/18/12/125006`.

[28] Nantakan Muensit. *Energy Harvesting with Piezoelectric and Pyroelectric Materials : Energy Harvesting with Piezoelectric and Pyroelectric Materials.* Trans Tech Publications, Limited, Zurich, SWITZERLAND, 2011. ISBN 9783038136583. URL `http://ebookcentral.proquest.com/lib/mcgill/detail.action?docID=1872572`.

[29] Chris R Bowen, Mengying Xie, Yan Zhang, Vitaly Yu. Topolov, and Chaoying Wan. Pyroelectric Energy Harvesting: Materials and Applications, 11 2018. URL `https://doi.org/10.1002/9783527807505.ch7`.

[30] Truls Norby and Ola Nilsen. Solid-state Electrochemistry. Technical report, University of Oslo, 2017.

[31] L Solymar and D Walsh. *Electrical properties of materials LK - https://mcgill.on.worldcat.org/oclc/430497036.* Oxford University Press, Oxford ; SE - xvi, 443 pages : illustrations ; 26 cm, 8th ed. edition, 2009. ISBN 9780199565924 0199565929 0199565910 9780199565917.

[32] Supriyo Datta. nanoHUB-U: Thermoelectricity: From Atoms to Systems, 2016. URL `https://nanohub.org/courses/TEAS`.

[33] Temesgen D Desissa. *Stability and properties of materials and interfaces for oxide thermoelectrics.* PhD thesis, University of Oslo, 2018.

[34] Ho Sung. Lee. *Thermal design : heat sinks, thermoelectrics, heat pipes, compact heat exchangers, ands solar cells.* Wiley, Hoboken, NJ SE - xviii, 630 pages : illustrations ; 25 cm, 2010.

[35] Matthias Schrade, Harald Fjeld, Truls Norby, and Terje G Finstad. Versatile apparatus for thermoelectric characterization of oxides at high temperatures. *The Review of scientific instruments*, 85(10):103906, 10 2014. ISSN 1089-7623 (Electronic). doi: 10.1063/1.4897489.

[36] Dinesh K Aswal, Ranita Basu, and Ajay Singh. Key issues in development of thermoelectric power generators: High figure-of-merit materials and their highly conducting interfaces with metallic interconnects. *Energy Conversion and Management*, 114:50–67, 2016. ISSN 0196-8904. doi: https://doi.org/10.1016/j.enconman.2016.01.065. URL `http://www.sciencedirect.com/science/article/pii/S0196890416300036`.

[37] G Jeffrey Snyder and Eric S Toberer. Complex thermoelectric materials. *Nature Materials*, 7(2):105–114, 2008. ISSN 1476-4660. doi: 10.1038/nmat2090. URL `https://doi.org/10.1038/nmat2090`.

[38] Hilaal Alam and Seeram Ramakrishna. A review on the enhancement of figure of merit from bulk to nano-thermoelectric materials. *Nano Energy*, 2(2):190–212, 2013. ISSN 2211-2855. doi: https://doi.org/10.1016/j.nanoen.2012.10.005. URL `http://www.sciencedirect.com/science/article/pii/S2211285512002078`.

[39] By Ali Shakouri. Thermoelectricity : From Atoms to Systems (Efficiency + Cost $ / W) Solar Cells We need to estimate the cost of TE system. pages 1–17, 2013.

[40] Temesgen D Desissa, Reidar Haugsrud, Kjell Wiik, and Truls Norby. Inter-diffusion across a direct p-n heterojunction of Li-doped NiO and Al-doped ZnO. *Solid State Ionics*, 320:215–220, 2018. ISSN 0167-2738. doi: https://doi.org/10.1016/j.ssi.2018.03.011. URL `http://www.sciencedirect.com/science/article/pii/S0167273817310597`.

[41] M G Cooper, B B Mikic, and M M Yovanovich. Thermal contact conductance. *International Journal of Heat and Mass Transfer*, 12(3):279–300, 1969. ISSN 0017-9310. doi: https://doi.org/10.1016/0017-9310(69)90011-8. URL `http://www.sciencedirect.com/science/article/pii/0017931069900118`.

[42] G Jeffrey Snyder. Application of the compatibility factor to the design of segmented and cascaded thermoelectric generators. *Applied Physics Letters*, 84(13):2436–2438,

3 2004. ISSN 0003-6951. doi: 10.1063/1.1689396. URL https://doi.org/10.1063/1.1689396.

[43] Terry Hendricks. ICT2018 presentation titled: Demonstrated High-Performance, High-Power Skutterudite Thermoelectric Modules for Space and Terrestrial Applications, 2018.

[44] G. Rogl and P. Rogl. Skutterudites, a most promising group of thermoelectric materials. *Current Opinion in Green and Sustainable Chemistry*, 4:50–57, 2017. ISSN 24522236. doi: 10.1016/j.cogsc.2017.02.006. URL http://dx.doi.org/10.1016/j.cogsc.2017.02.006.

[45] Serge Bédard. Waste Heat to Power. pages 1341–1350, Toronto, 2009. CanmetENERGY. doi: 10.1002/9781119117896.ch112.

[46] Elliot Woolley, Yang Luo, and Alessandro Simeone. Industrial waste heat recovery: A systematic approach. *Sustainable Energy Technologies and Assessments*, 29:50–59, 2018. ISSN 2213-1388. doi: https://doi.org/10.1016/j.seta.2018.07.001. URL http://www.sciencedirect.com/science/article/pii/S2213138818301012.

[47] Daniel Champier. Thermoelectric generators: A review of applications. *Energy Conversion and Management*, 140:167–181, 2017. ISSN 0196-8904. doi: https://doi.org/10.1016/j.enconman.2017.02.070. URL http://www.sciencedirect.com/science/article/pii/S0196890417301851.

[48] Saed A Musmar, N Razavinia, Frank Mucciardi, and Iskander Tlili. Performance analysis of a new Waste Heat Recovery System. *Int. J. Therm. Envir. Eng*, 10:31–36, 2015.

[49] B. Orr, A. Akbarzadeh, and P. Lappas. An exhaust heat recovery system utilising thermoelectric generators and heat pipes. *Applied Thermal Engineering*, 126:1185–1190, 2017. ISSN 13594311. doi: 10.1016/j.applthermaleng.2016.11.019. URL http://dx.doi.org/10.1016/j.applthermaleng.2016.11.019.

[50] P. Aranguren, D. Astrain, A. Rodríguez, and A. Martínez. Net thermoelectric power generation improvement through heat transfer optimization. *Applied Thermal Engi-*

neering, 120:496–505, 2017. ISSN 13594311. doi: 10.1016/j.applthermaleng.2017.04.022. URL http://dx.doi.org/10.1016/j.applthermaleng.2017.04.022.

[51] M. Araiz, A. Martínez, D. Astrain, and P. Aranguren. Experimental and computational study on thermoelectric generators using thermosyphons with phase change as heat exchangers. *Energy Conversion and Management*, 137:155–164, 2017. ISSN 01968904. doi: 10.1016/j.enconman.2017.01.046. URL http://dx.doi.org/10.1016/j.enconman.2017.01.046.

[52] P. Aranguren, M. Araiz, and D. Astrain. Auxiliary consumption: A necessary energy that affects thermoelectric generation. *Applied Thermal Engineering*, 141(September 2017):990–999, 2018. ISSN 13594311. doi: 10.1016/j.applthermaleng.2018.06.042.

[53] Song Lv, Wei He, Qingyang Jiang, Zhongting Hu, Xianghua Liu, Hongbing Chen, and Minghou Liu. Study of different heat exchange technologies influence on the performance of thermoelectric generators. *Energy Conversion and Management*, 156 (November 2017):167–177, 2018. ISSN 01968904. doi: 10.1016/j.enconman.2017.11.011.

[54] D A Reay, P A Kew, and R J McGlen. Chapter 3 - Heat pipe components and materials. pages 65–94. Butterworth-Heinemann, Oxford, 2014. ISBN 978-0-08-098266-3. doi: https://doi.org/10.1016/B978-0-08-098266-3.00003-0. URL http://www.sciencedirect.com/science/article/pii/B9780080982663000030.

[55] Guohui Zheng. A novel flow-modified heat pipe-development and experimental investigation /. 1 2005.

[56] TECTEG. Low (DT) Thermoelectric Harvesting TEG Power Module. URL https://tecteg.com/low-dt-thermoelectric-harvesting-teg-power-module/.

[57] D A Reay, Peter Kew, P D Dunn, and Ryan McGlen. *Heat Pipes : Theory, Design and Applications*. Elsevier Science & Technology, Jordan Hill, UNITED KINGDOM, 2006. ISBN 9780080464770.

[58] F. Mucciardi, J. Gruzleski, G. Zheng, Z. Chunhui, and Z. Yuan. Heat pipe, 2002. URL https://patents.google.com/patent/WO2003071215A1/en.

[59] Gerard Campeau. RAW ALLOYED TEG POWER MATERIAL AVAILABLE IN P & N- TYPE. URL `https://thermoelectric-generator.com/wp-content/uploads/2014/07/Ingot-Raw-Material-BiTe-N-and-P.pdf`.

[60] Suhas V Patankar. *Numerical heat transfer and fluid flow*. Hemisphere Pub. Corp. ;, Washington, 1980. ISBN 0070487405 9780070487406 0891165223 9780891165224.

[61] Aidan Wimshurst. Fluid mechanics 101: The k-epsilon turbulence model.

[62] Milovan Peric. Flow simulation using control volumes of arbitrary polyhedral shape. *ERCOFTAC Bulletin*, 62:25–29, 1 2004.

[63] J P Holman. *Heat transfer*. McGraw Hill Higher Education, Boston [Mass.] SE - xxii, 725 pages : illustrations ; 26 cm., 10th ed. edition, 2010. ISBN 9780073529363 0073529362 9780071267694 0071267697.

[64] Yunus A Cengel and Michael A Boles. *Thermodynamics : an engineering approach LK - https://mcgill.on.worldcat.org/oclc/869741544*. McGraw-Hill Education, New York SE - xxvi, 996 pages : illustrations ; 26 cm, eighth edi edition, 2015. ISBN 9780073398174 0073398179.

[65] Ankit Rohatgi. WebPlotDigitizer Version 4.2, 2019. URL `https://automeris.io/WebPlotDigitizer`.

[66] Joao Ramos, Alex Chong, and Hussam Jouhara. Experimental and numerical investigation of a cross flow air-to-water heat pipe-based heat exchanger used in waste heat recovery. *International Journal of Heat and Mass Transfer*, 102:1267–1281, 2016. ISSN 0017-9310. doi: https://doi.org/10.1016/j.ijheatmasstransfer.2016.06.100. URL `http://www.sciencedirect.com/science/article/pii/S0017931016303982`.

[67] Alexander S Rattner and Tyler J Meehan. Simple analytic model for optimally sizing thermoelectric generator module arrays for waste heat recovery. *Applied Thermal Engineering*, 146:795–804, 2019. ISSN 1359-4311. doi: https://doi.org/10.1016/j.applthermaleng.2018.10.003. URL `http://www.sciencedirect.com/science/article/pii/S1359431118305210`.

[68] Marcos Compadre Torrecilla, Andrea Montecucco, Jonathan Siviter, Andrew Strain, and Andrew R Knox. Transient response of a thermoelectric generator to load steps

under constant heat flux. *Applied Energy*, 212:293–303, 2018. ISSN 0306-2619. doi: https://doi.org/10.1016/j.apenergy.2017.12.010. URL http://www.sciencedirect.com/science/article/pii/S0306261917317233.

[69] John R Taylor. *An introduction to error analysis*. University Science Books, Sausalito, Calif. SE - xvii, 327 pages : illustrations ; 26 cm, 2nd ed. edition, 1997.

[70] Bent Sørensen. Renewable energy : physics, engineering, environmental impacts, economics and planning - https://mcgill.on.worldcat.org/oclc/992170112, 2017.

[71] Vahe Tshitoyan, John Dagdelen, Leigh Weston, Alexander Dunn, Ziqin Rong, Olga Kononova, Kristin A. Persson, Gerbrand Ceder, and Anubhav Jain. Unsupervised word embeddings capture latent knowledge from materials science literature. *Nature*, 571(7763):95–98, 2019. ISSN 14764687. doi: 10.1038/s41586-019-1335-8. URL http://dx.doi.org/10.1038/s41586-019-1335-8.

[72] Philip Nuss and Matthew J. Eckelman. Life cycle assessment of metals: A scientific synthesis. *PLoS ONE*, 9(7):1–12, 2014. ISSN 19326203. doi: 10.1371/journal.pone.0101298.

[73] Saniya Leblanc, Shannon K. Yee, Matthew L. Scullin, Chris Dames, and Kenneth E. Goodson. Material and manufacturing cost considerations for thermoelectrics. *Renewable and Sustainable Energy Reviews*, 32:313–327, 2014. ISSN 13640321. doi: 10.1016/j.rser.2013.12.030. URL http://dx.doi.org/10.1016/j.rser.2013.12.030.

[74] McMaster-Carr. Compression Springs, . URL https://www.mcmaster.com/catalog/125/1326.

[75] McMaster-Carr. Single-Turn Spiral Internal Retaining Rings, . URL https://www.mcmaster.com/catalog/125/3406.

[76] McMaster-Carr. 304 Stainless Steel Wire Cloth, . URL https://www.mcmaster.com/9226T966.

[77] Corsair. Air Series™ AF120 LED Purple Quiet Edition High Airflow 120mm Fan. URL https://www.corsair.com/ca/en/Categories/Products/Fans/AIR-SERIES-LED-CONFIG/p/CO-9050015-PLED.

[78] Adafruit. INA219 High Side DC Current Sensor Breakout - 26V 3.2A Max. URL https://www.adafruit.com/product/904.

[79] OMEGA. Thermally Conductive Epoxies and Thermally Conductive Grease. URL https://www.omega.ca/en/sensors-and-sensing-equipment/sensing-accessories/adhesives-and-paste/p/OB-100-OB-200-OT-200.

[80] SKF. Mityvac: Hand Pumps Kits. URL https://www.skf.com/mityvac/products/hand-vacuum-pressure-pumps-kits-accessories/hand-pump-kits/index.html.

[81] Reflectix Inc. Reflective Technology Performance Information. URL https://www.reflectixinc.com/about-reflective-technology/performance-information/.